2007-03-20

Effects of Spanwise and Discrete Disturbances on Separating Boundary Layers on Low Pressure Turbine Blades

Daniel D. Reimann
Brigham Young University - Provo

EFFECTS OF SPANWISE AND DISCRETE DISTURBANCES ON SEPARATING BOUNDARY LAYERS ON LOW PRESSURE TURBINE BLADES

by

Daniel D. Reimann

A thesis submitted to the faculty of

Brigham Young University

in partial fulfillment of the requirements for the degree of

Master of Science

Department of Mechanical Engineering

Brigham Young University

April 2007

BRIGHAM YOUNG UNIVERSITY

GRADUATE COMMITTEE APPROVAL

of a thesis submitted by

Daniel D. Reimann

This thesis has been read by each member of the following graduate committee and by majority vote has been found to be satisfactory.

Date	Jeffrey P. Bons, Chair
Date	R. Daniel Maynes
Date	Scott L. Thomson

BRIGHAM YOUNG UNIVERSITY

As chair of the candidate's graduate committee, I have read the thesis of Daniel D. Reimann in its final form and have found that (1) its format, citations, and bibliographical style are consistent and acceptable and fulfill university and department style requirements; (2) its illustrative materials including figures, tables, and charts are in place; and (3) the final manuscript is satisfactory to the graduate committee and is ready for submission to the university library.

Date

Jeffrey P. Bons
Chair, Graduate Committee

Accepted for the Department

Matthew R. Jones
Graduate Coordinator

Accepted for the College

Alan R. Parkinson
Dean, Ira A. Fulton College of Engineering and Technology

ABSTRACT

EFFECTS OF SPANWISE AND DISCRETE DISTURBANCES ON SEPARATING BOUNDARY LAYERS ON LOW PRESSURE TURBINE BLADES

Daniel D. Reimann

Department of Mechanical Engineering

Master of Science

Flow measurements were made on two highly loaded, low pressure turbine blade configurations in a low-speed, linear cascade facility. The L1M blade has a design Zweifel coefficient of 1.34 with a peak cp near 47% c_x (mid-loaded) and the Pack B blade has a design Zweifel coefficient of 1.15 with a peak cp at 63% c_x (aft-loaded). Flow velocity and surface pressure measurements were taken for Re_c=20,000 and 3% inlet freestream turbulence. For these operating conditions, a large separation bubble forms on the blade suction surface, beginning at 59% c_x and reattaching at 86% c_x on the L1M blade and a non-reattaching bubble beginning at 68% c_x on the Pack B. A spanwise row of discrete vortex-generating jets located at 59% c_x on the Pack B and 50% c_x on the L1M were used as a separation control device and were pulsed at a frequency of 5 Hz with a duty cycle of 25%. The Pack B with its open separation bubble proved to be a

better candidate for VGJ control than the L1M with its closed separation bubble. Further studies were made on the Pack B blade comparing wake and VGJ effects. A wake generator was used to simulate the periodic passing of upstream wakes through the blade passage for the Pack B configuration. The wake passing frequency of 4.5Hz was set to match a typical engine flow coefficient for a low pressure turbine ($\phi = 0.85$). Data were taken using PIV and a hot-film anemometer mounted on a blade following device. Velocity, turbulence, and intermittency measurements were made along the suction surface of the blade to characterize the bubble dynamics and transitional behaviors for both the presence of unsteady wakes and pulsing VGJs. The wakes caused early breakdown of the separated free shear layer resulting in a thinning of the separation region. The VGJs caused an upstream disturbance which convects downstream, temporarily pushing off the separation bubble. Overall, both wakes and VGJs suppress the size of the steady-state separation bubble, though through different mechanisms. Three-dimensional aspects of the jet disturbance are studied by investigating the effects of the VGJs at two spanwise locations.

ACKNOWLEDGMENTS

I am truly grateful for the opportunity I have had to work on this project with my advisor Dr. Jeffrey Bons. He is an outstanding mentor and is always uplifting and encouraging. The advice and lessons he has taught me are invaluable and have made me not just a better engineer but a better person.

It has also been a great privilege to work closely with my good friend Matthew Bloxham. Working together with Matt has made the long hours in the lab fun an enjoyable. I believe that by working together we were able to find better solutions to many of the problems we encountered than had we been working individually.

I would like to thank my friends Jon Pluim, Katie Crapo George, and Mike Armstrong. Without their able assistance and continual help this research would not have been possible. Many thanks go to Kevin Cole and Ken Forrester of the Mechanical Engineering Department for their brilliant ideas and resolutions to many technical issues. I would also like to acknowledge the Air Force Office of Scientific Research and LtCol Rhett Jeffries as program manager for the financial support of this research.

Finally I would like to thank my beautiful wife Jill. Her continual love and support have greatly enriched my life.

TABLE OF CONTENTS

LIST OF FIGURES

NOMENCLATURE

B	VGJ blowing ratio, (U_{jet}/U_{local})
L	distance between wake generator rods
Re_c	Re based on cascade inlet conditions, $c_x U_{in}/\nu$
S	blade spacing
T	period
U	velocity magnitude
VGJ	vortex generator jet
c_p	pressure coefficient, $(P_{Tin}-P_{local})/(P_{Tin}-P_{Sin})$
c_x	blade axial chord (0.238m)
d	VGJ hole diameter
f	VGJ pulse frequency [Hz]
f_{HP}	high-pass filter cutoff frequency [Hz]
f_{LP}	low-pass filter cutoff frequency [Hz]
u	instantaneous streamwise velocity component
u’	fluctuating component of velocity
u_{mean}	mean streamwise velocity component
u_{rms}	root mean square streamwise velocity component
$\tilde{u}$	ensemble average streamwise velocity
t	time
x	axial coordinate from the cascade inlet face
y	local surface normal coordinate
z	spanwise coordinate
Γ	intermittency distribution
ϕ	$U_{in,axial}/U_{rod}$
ν	kinematic viscosity
γ	intermittency

subscripts

S	static
T	total
axial	axial direction
in	cascade inlet
inf	average freestream velocity through cascade
jet	VGJ data set
local	local freestream conditions
max	maximum value in full cycle
rod	wake generator rod
wake	wake data set

1 Introduction

1.1 Background

Low-pressure turbines (LPT) are continually being designed with increased loading for better stage performance. Inherent to higher blade loading is an increased tendency for boundary layer separation, particularly at low Reynolds numbers when the boundary layers are laminar. Matsunuma et al. and Sharma have shown dramatic increases in stage losses associated with boundary layer separation [1,2]. In order to reduce the losses due to separation, a variety of different passive and active control methods have been studied [3-5]. Of the different control methods studied, one that has shown considerable promise is vortex generating jets (VGJs). VGJs are an active control system which have the potential benefit of being able to turn on or off according to their need. VGJs have been studied in both steady and pulsing operation. Steady VGJ operation induces streamwise vortices which pull high momentum freestream fluid into the low momentum separation region and effectively reduce losses due to separation [6-9]. Pulsing VGJs have also shown to be very effective at reducing the separation losses but with a fraction of the mass flow requirements [8]. This makes implementation into a real engine much more practical. However, the control mechanism for these pulsed VGJs is not fully understood. Numerical investigations by Postl et al. [10,11] suggest that for

pulsed VGJs the dominant mechanism for control is boundary layer by-pass transition rather than streamwise vortices.

The LPT environment, which includes high freestream turbulence and the periodic passing of wakes from the previous blade row, also has a very significant impact on the separation dynamics [12]. Many studies are now looking at the effectiveness of control methods in an unsteady environment with the periodic passing of wakes. Wakes themselves have proven to offer benefits by reducing separation size and acting as a form of flow control. PIV studies by Stieger et al. [13] identified the presence of coherent vortices in the separated boundary layer and proposed their formation to be caused by the passing of wakes over an inflexional boundary layer. Gostelow and Thomas [14,15] also performed wake studies using a flat plate with a separated boundary layer caused by an imposed pressure distribution. Using hot-wire measurements they found that the wake stabilizes the boundary layer, leaving behind a region of calmed flow evidenced by boundary layer profiles, turbulence plots, and intermittency plots. Similar results were also seen by Funazaki et al. [16,17], Cattanei et al. [18], and Zhang et al. [3,4].

Transition plays a critical role in the separation dynamics associated with LPTs. For the majority of flow control methods studied by researchers, transition is the dominating phenomenon responsible for reattachment or suppression of a separated boundary layer. Mayle [19] provides a good discussion of the role and modes of laminar-turbulent transition on turbomachinery blading, including the influence of unsteady wakes on separated boundary layers. Many of the previously mentioned researchers have further substantiated the influence of transition in separation dynamics. In order to characterize the transition dynamics, higher order turbulent statistics as well as

intermittency are often used. However, intermittency is not a straight forward measurement, and different methods have been used as a means of measuring intermittency in a transitioning flow. One successful algorithm for measuring intermittency was developed by Volino et al. [20]. This method uses filtering and the absolute value of the first and second derivatives of the velocity signal as turbulence discriminators to determine intermittent behaviors associated with the flow at a location.

1.2 Objective

The objective of this thesis is to compare the dynamic and transitional influences of VGJs and unsteady wakes on a separation bubble on LPTs. VGJs are studied on two different LPT profiles in order to compare their influence on both an aft-loaded blade with a separating, non-reattaching boundary layer, and a mid-loaded blade with a separating, reattaching boundary layer. This is done in order to find the LPT profile which exhibits the greater separation. The LPT with the greater separation is then used to compare the influence of discrete VGJs and spanwise wakes on the separated boundary layer as well as the role that VGJs and wakes have on transition.

2 Experimental Facility

2.1 Wind Tunnel

An open-loop wind tunnel driven by a centrifugal blower is used. The flow passes through a series of perforated plates, honeycomb, and screens which condition the flow to a ±2% velocity uniformity and 0.3% freestream turbulence. The level of freestream turbulence is then augmented to 3% turbulence with a passive square-bar grid located 5 axial chords (c_x) upstream of the two passage linear cascade. The flow was found to be fairly isotropic (all three fluctuating components of velocity within ±10% of each other) with an integral length scale of 2 cm at the cascade inlet plane. Acceleration through the cascade causes the freestream turbulence to drop below 2% at the exit and the length scale to increase to nearly 3 cm. A more detailed description of the cascade facility can be found in Eldredge and Bons [8].

The test section consists of a two passage linear cascade containing either the Pratt & Whitney Pack B turbine blade profile or the L1M turbine blade profile which was recently designed at the Air Force Research Laboratory by Clark [21]. A schematic of the cascade with the Pack B blades is shown in Figure 2-1. The Pack B blade is an aft-loaded blade with an axial chord of 0.238 m, a span of 0.38 m, a design Zweifel load coefficient of 1.15, and a solidity (axial chord/spacing) of 1.14. The L1M blade has an

axial chord of 0.22 m, a span of 0.38 m, a solidity of 0.99, a Zweifel coefficient of 1.34, and is a mid-loaded blade. Both blades have identical inlet and exit angles, so they are interchangeable in the cascade. Tests were run at Re_c=20,000 for both blade profiles. At these conditions the Pack B has a non-reattaching separation bubble beginning near 68% c_x, while the L1M has a reattaching separation bubble from about 59% c_x to 82% c_x.

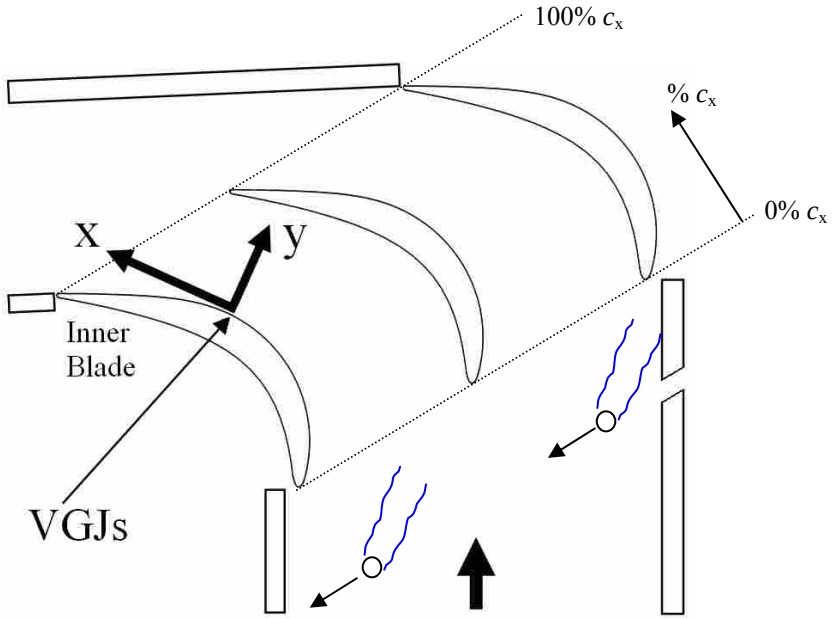

Figure 2-1: Linear Cascade with Pack B profiles and upstream wake generator

Pressure coefficient (c_p) distributions are validated for both blade configurations by pressure taps on the suction surface of the inside blade and on the pressure surface of the middle blade. The Pack B configuration contains 13 suction surface taps and 7 pressure surface taps while the L1M has 14 suction surface taps and 7 pressure surface taps. The c_p profiles are measured by connecting the pressure taps to a 0.1" H_2O Druck differential pressure transducer referenced to a pitot tube located upstream of the cascade inlet. The c_p distributions are compared to 2D viscous solvers labeled VBI [22] for the

Pack B configuration and MISES for the L1M configuration [23]. All c_p and velocity data were taken over the center 0.15 m of blade span, where the flow was confirmed to be approximately two-dimensional.

The VGJs are located on the suction surface of the inner blade of the cascade and are 2.6 mm in diameter for the Pack B and 2.3 mm in diameter for the L1M. The jets are spaced 10 diameters apart along the span of the blade at 59% c_x for the Pack B and 50% c_x on the L1M. These locations were selected to be near the peak c_p location for the respective blades. The jets are injected into the flow at a 30 degree pitch angle from the blade surface and a 90 degree skew angle from the streamwise direction (see inset of Figure 2-2). The jets are connected to a pressure cavity in the blade which is connected to high pressure air with a pressure regulator to regulate the exit velocity of the VGJs and a solenoid valve which pulses the jets. The jets are pulsed at a frequency of 5 Hz with a duty cycle of 25%. The jet blowing ratio is operated near B_{max}=1.8 for the L1M and 2.1 for the Pack B, where the blowing ratio is defined as the ratio of jet exit velocity to the local freestream velocity (U_{jet}/U_{local}). The VGJ velocity profiles were measured by a single element hot-film anemometer as the jets exited into a quiescent environment. The jet pulse histories are shown in Figure 2-2. The jet pulse histories are nearly a step function with an initial oscillation attributed to initial air compression within the pressurized cavity.

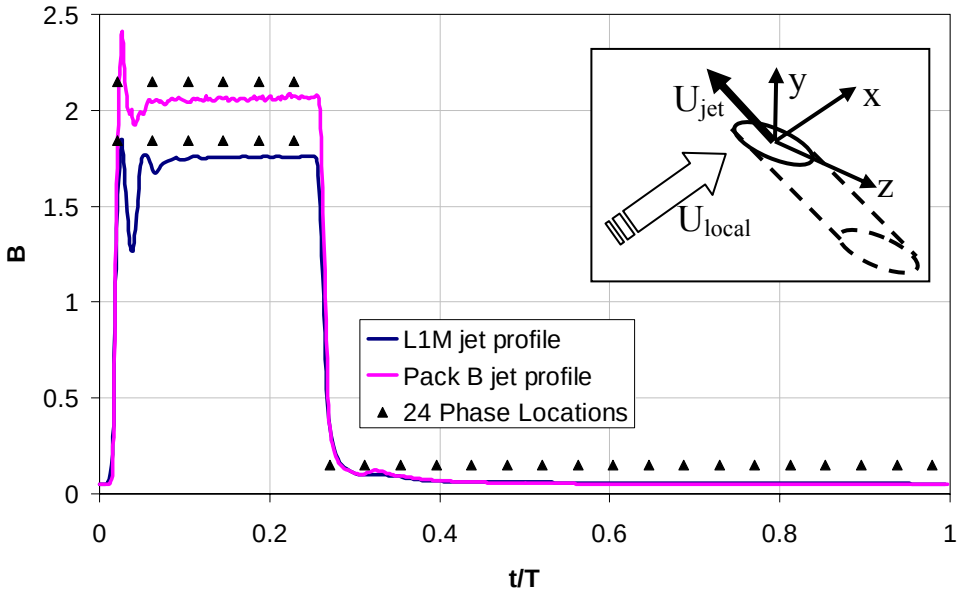

Figure 2-2: VGJ pulse history for L1M and Pack B with 24 phase markings, with inset VGJ orientation

2.2 Wake Generator

A wake generator is located 12.7 cm (0.53 c_x) upstream of the cascade inlet (Figure 2-1). Wakes are created from 4 mm carbon fiber rods and pass through the tunnel normal to the axial direction of the cascade. The rods are spaced at L/S=1.64 where L is the distance between rods and S is the blade spacing. This is meant to simulate the unsteady wakes caused by stator vanes crashing across the rotor blades since a stator vane count is typically 60-75% of the rotor blade count. The rods are oriented in the spanwise direction and are attached to a chain sprocket system which is powered by a variable frequency motor. The speed of the rods are controlled to maintain a flow coefficient of φ=0.85 with ±3% fluctuation. The period between rods was measured to be about 225 ms which is very close to the pulsing period of the VGJs of 200 ms. Low density foam is used to guide the tip and the base of the rods through the tunnel, dampen

rod vibrations, and seal the tunnel. Synchronization of rod period and data acquisition are accomplished with the use of an optical sensor which detects the passing of the rods as they exit the tunnel. A drawing of the wake generator can be seen in Figure 2-3.

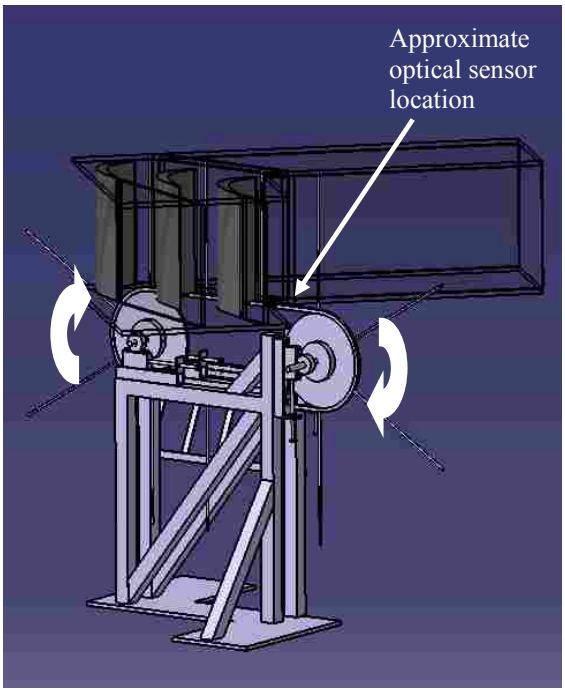

Figure 2-3: CAD model of the wake generator and tunnel test section

2.3 Instrumentation

The primary tool for data acquisition is a single element hot-film anemometer. The hot-film element has a diameter of 50.8 μm, a length of 1.02 mm, and a frequency response of about 200 kHz. The hot-film mounts to a blade following device which allows a traverse to move the blade follower in a linear direction while the blade follower keeps the hot-film at a constant distance from the blade surface, spanning most of the blade suction surface at a single spanwise location. Sixteen streamwise profiles were obtained with wall distances between 1.2 mm and 20.0 mm from the blade surface. Each

profile consists of 64 measurement locations with spacing ranging between 2.7 mm and 6.9 mm. The smaller spacing is clustered in the region of highest near wall velocity gradients. The uncertainty in velocity measurements is ±0.03 m/s, and the follower y-position is accurate to within ±0.2 mm.

Data were also collected using a Particle Imaging Velocimetry (PIV) system on the Pack B blade. The PIV system is mounted to a three-axis traverse and is located below the test section. A Nd: YAG laser consecutively projects two 1 mm thick laser sheets in the x-y plane (see inset to Figure 2-1) which are separated by a time delay of 250 μs. Olive oil is used to seed the flow with particles ranging in diameter between 1 and 2 μm. A high speed digital camera is positioned below the test section with a resolution of 1376 by 1040 pixels. The single camera requires both an upstream and a downstream window to capture the flow along the desired region of the blade. The upstream window covers from ~50% c_x to ~81% c_x while the downstream window covers from ~80% c_x to ~100% c_x with about 6 mm of overlap. These windows are later merged together to create one continuous set of data as shown in Figure 2-4. Measurements were taken spanning one VGJ hole pitch (10d) at 18 spanwise (z) locations for the VGJ data and 6 spanwise locations for the wake conditions. Fewer spanwise locations were taken for the wake data due to the two-dimensional nature of the wake influence on the separation bubble. It should be noted that all PIV velocity data is presented according to the camera coordinate system. Since the region of interest (separation zone) on the suction surface of the blade is relatively flat and aligned with the camera window, the x and y camera coordinates are approximately the same as the freestream and wall-normal directions (see Figure 2-4).

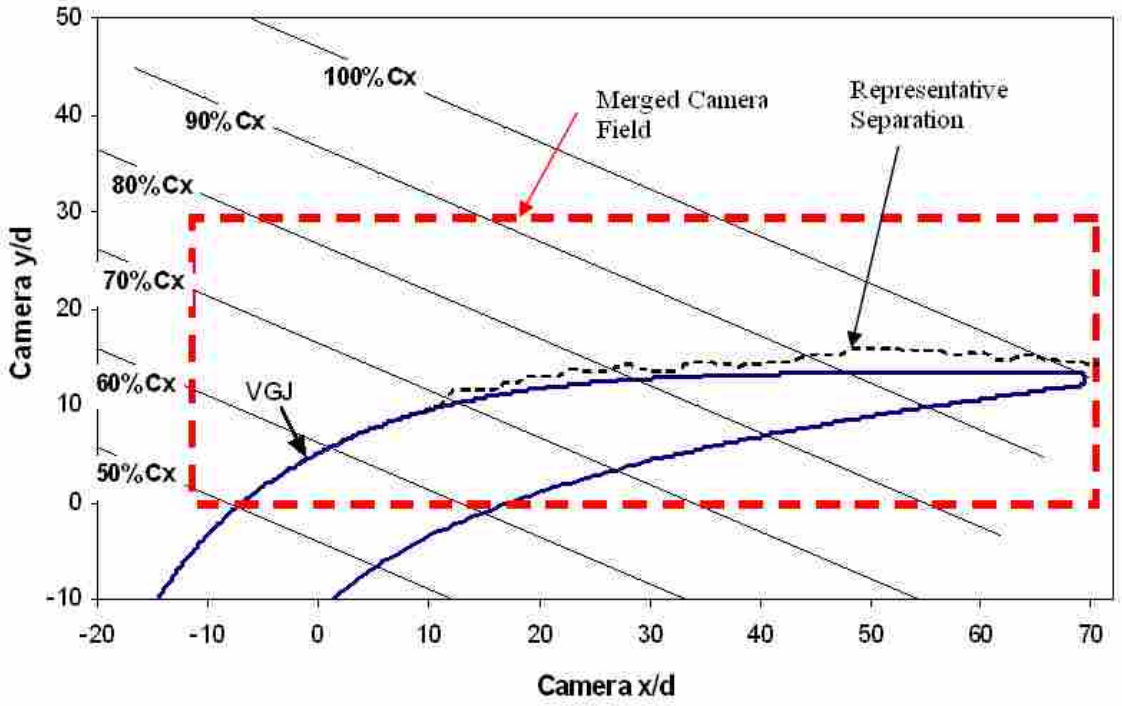

Figure 2-4: Merged upstream and downstream data windows oriented on Pack B blade

2.4 Data Processing

For the hot-film follower data, large data records are taken at each location to ensure steady statistics for turbulence measurements. At each position data are acquired for 16 seconds at a frequency of 10 kHz (160,000 data points) for the no control case, while for the VGJ and wake conditions data are acquired for 24 seconds at a frequency of 10 kHz (240,000 data points) at each location. The data are phase-locked using a TTL signal from the pulsed valve controller for the VGJ data while for the wake data the phase-locking is accomplished by means of an optical sensor which detects the passing of a wake generating rod. The data processing procedure is shown schematically in Figure 2-5 and is used for both VGJ and wake conditions. The cycle count varies between VGJ and wake conditions since the periods are slightly different (T_{wake} = 225 ms while T_{jet} =

200 ms). Although the data processing is the same for both the VGJ and wake data, only the VGJ case will be described. First, 120 cycles (24 seconds x 5 Hz) of velocity data are averaged together to produce a mean velocity distribution ($\tilde{u}$) at each location. This ensemble average is then subtracted from each of the 120 cycles to eliminate bulk unsteady motion in the flow, leaving the fluctuating component of the velocity history. Each cycle of the fluctuating component of the velocity history is then divided up into 24 phases of equal length (8.3 ms). Then the first phase from each of the 120 cycles is concatenated together to form one continuous velocity deviation signal ($u - \tilde{u}$) associated with the first 8.3 ms of the cycle history (a total of 10,000 data points). This last step is performed for each of the remaining 23 phases resulting in velocity and turbulence statistics histories throughout the cycle.

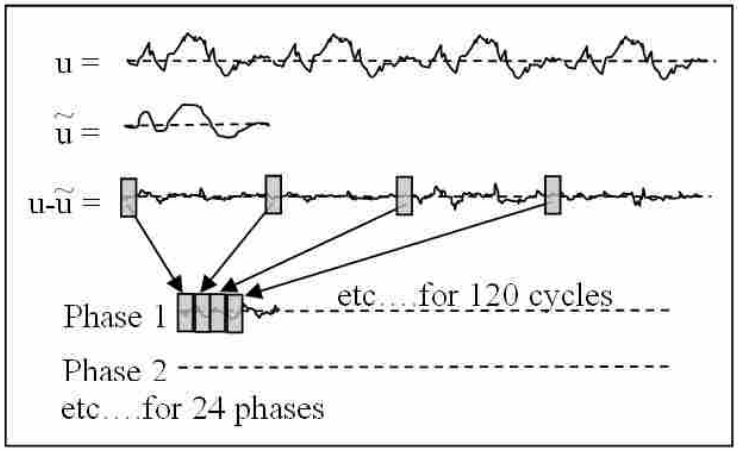

Figure 2-5: Data processing flow chart for phase-locked unsteady data from hot-film

3 Intermittency Discriminator

Laminar to turbulent transition plays a major role in controlling separation on an LPT. Early transition can result from the passing of wakes as well as the activation of VGJs. In order to understand the transitional effects of VGJs and wakes, intermittency is used as the principle transition indicator. Intermittency (γ) is determined at discrete points in the flow and is defined as the percentage of time that the velocity history is turbulent. Figure 3-1 is a diagram of a velocity history in a transitioning flow with both laminar and turbulent segments. Since 25% of the velocity history in Figure 3-1 is turbulent, the intermittency is γ=0.25. In addition, higher order statistics are also computed from the velocity histories, namely skewness, kurtosis, and kurtosis of the first derivative of the velocity. Other researchers have also used higher order statistics as a method of determining regions of transition. Cattanei et al. [18] utilized skewness as a transition indicator in a turbomachinery flow, and Townsend [24] found the kurtosis of the velocity derivative to be a useful indication of transition. These higher order statistics have shown to be useful as transition indicators and for validating the intermittency results.

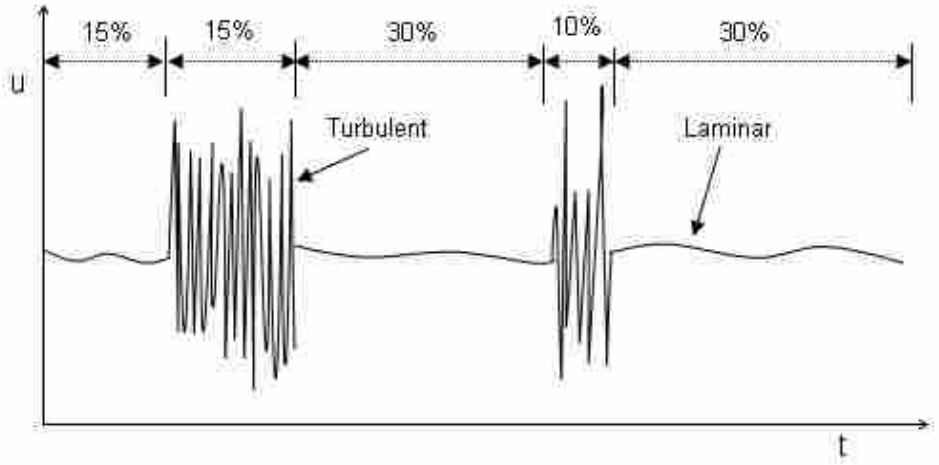

Figure 3-1: Schematic of an intermittent velocity history with γ=0.25.

3.1 Software Development

In order to determine the intermittency value of the flow at a given location, a LabView program was written following the method presented by Volino et al. [20]. Only slight modifications were made to the methodology developed by Volino. The LabView program has been included in Appendix A. An outline of the intermittency calculation is presented below followed by a step by step explanation.

1. $f_{HP} = 100*u_{mean}$
2. $\Gamma_1 = 1$ if $|du/dt| > 19.95*u_{mean}$

   $\Gamma_1 = 0$ otherwise
3. $\Gamma_2 = 1$ if $|d^2u/dt^2| >$ Threshold(Γ_2) → ($\Gamma_1 = \Gamma_2$)
4. $\Gamma_3 = 1$ if $\Gamma_1 = 1$ or $\Gamma_2 = 1$

   $\Gamma_3 = 0$ otherwise
5. $f_{LP} = 17.78*u_{mean}$

6. $\Gamma_4 = 1$ if $\Gamma_3 > 0.5$

   $\Gamma_4 = 0$ otherwise

First, a hot-film is used to measure the velocity history at a frequency of 10 kHz for 24 seconds for the VGJ and wake conditions. The velocity history is then high-pass filtered with a cutoff frequency of $f_{HP}=100*u_{mean}$ (step 1) in order to eliminate low-frequency fluctuations common to laminar and turbulent flows, with f_{HP} values typically ranging between 30 and 200 Hz. Then the absolute value of the first time derivative of the velocity history is compared to a predetermined threshold (step 2) yielding a Γ_1 distribution which is the first intermittency discriminator. A second intermittency discriminator (Γ_2) is computed from the second time derivative of the velocity history (step 3). The value of "Threshold(Γ_2)" is selected such that the integral of Γ_1 over time is equal to the integral of Γ_2 over time. The first and the second intermittency discriminators are then combined to yield a third distribution Γ_3 where Γ_3 is equal to 1 at any given time if either Γ_1 or Γ_2 are equal to 1 at that time (step 4). This third intermittency discriminator is then low-pass filtered (step 5) to eliminate any erratic transitions between the two states (0 and 1). The filtered Γ_3 distribution results in a Γ_4 distribution (step 6) which is integrated over time to yield a final intermittency value γ for the flow at the current location. The only modification made to the original Volino method was to calculate the high and low-pass filter cutoff frequencies using u_{mean} rather than the freestream velocity (u_{inf}). This was done to more closely relate the cutoff frequencies to the local convective speed of the flow disturbances over the hot-film anemometer, thus avoiding erroneous intermittency values in or near the separation region.

3.2 Flat Plate Validation

In order to validate the methodology for determining intermittency, boundary layer studies were performed in a naturally transitioning boundary layer on a flat plate as depicted in Figure 3-2.

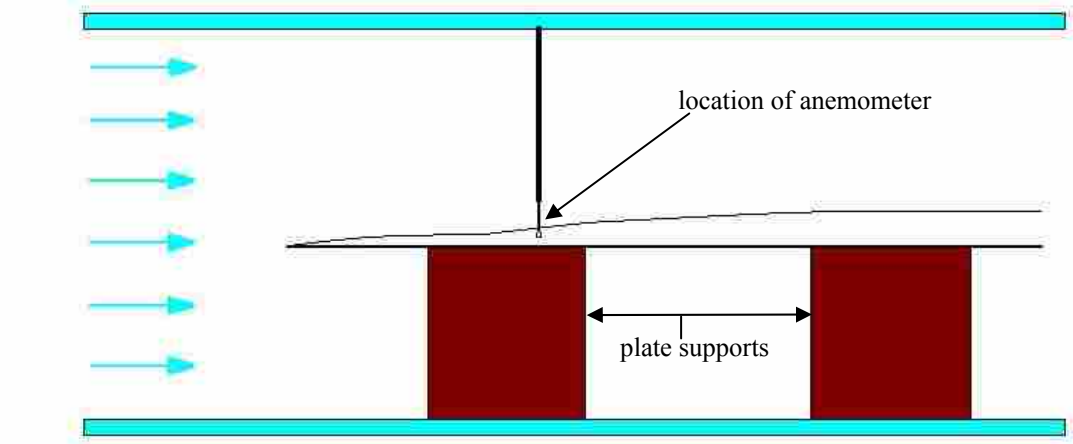

Figure 3-2: Flat plate configuration for intermittency validation studies

A hot-film was placed in the transition region of the boundary layer and recorded velocity histories at a sample rate of 10 kHz for 2 seconds for each velocity history. These velocity measurements were saved and loaded individually into the intermittency program so that intermittency threshold values could be optimized. The intermittency threshold values which were studied for optimization were the high-pass filtering frequency, the Γ_1 threshold value, and the low-pass filtering frequency. After changing these values for multiple velocity records it was determined that the intermittency calculation was not significantly affected by changes to the Γ_1 threshold value and the low-pass filtering frequency, but that the high-pass filtering frequency did have a significant influence on the final intermittency value. Volino [20] used a high-pass filter

cutoff frequency of $f_{HP}=200*u_{inf}$ where 200 is the filter coefficient. Rather than basing the high-pass filter frequency on the average freestream velocity (u_{inf}) it was decided to use the local mean velocity (u_{mean}) which together with a filter coefficient of 100 yielded the best results. The intermittency program's ability to identify laminar and turbulent zones in the velocity history was determined by plotting the fluctuating component of velocity (u') together with the Γ_4 distribution. Figure 3-3 through Figure 3-6 contain u' vs. Γ_4 distributions at 4 different levels of intermittency. Γ_4 is set to 0 (low) through laminar zones and 1 (high) for turbulent zones for the intermittency calculation. The scale for the Γ_4 distributions are on the right side of each graph in Figure 3-3 through Figure 3-6. Velocity data were also acquired using a 4 μm diameter hot-wire instead of the larger 25 μm hot-film since the hot-wire has a higher frequency response. The intermittency algorithm worked equally well for these data without adjusting any of the parameters.

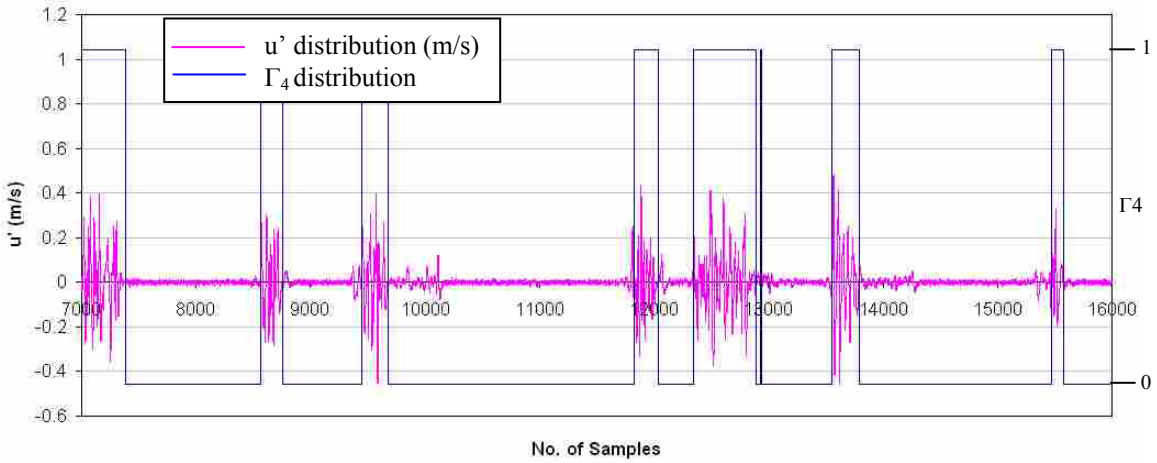

Figure 3-3: u' and Γ_4 distributions for an intermittency value of γ =0.2

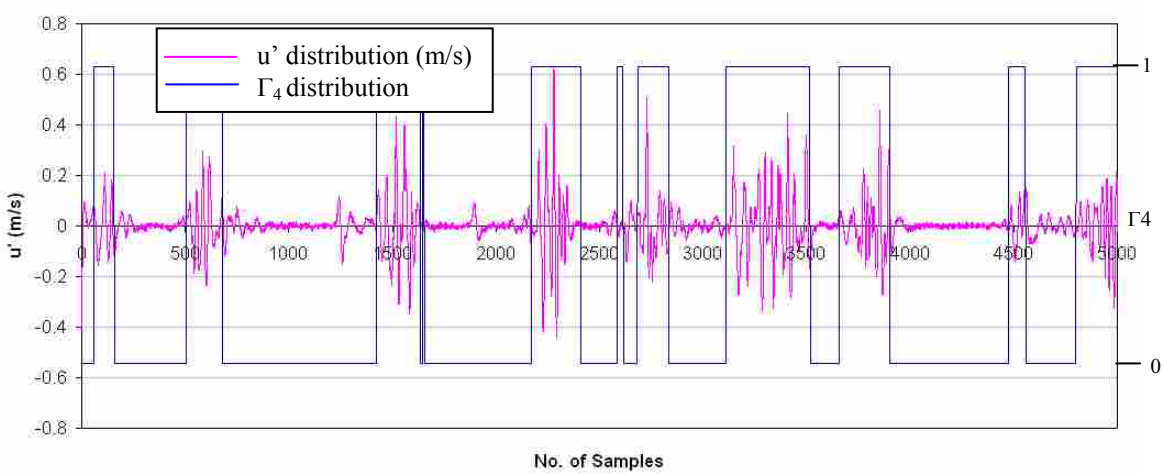

Figure 3-4: u' and Γ_4 distributions for an intermittency value of γ =0.32

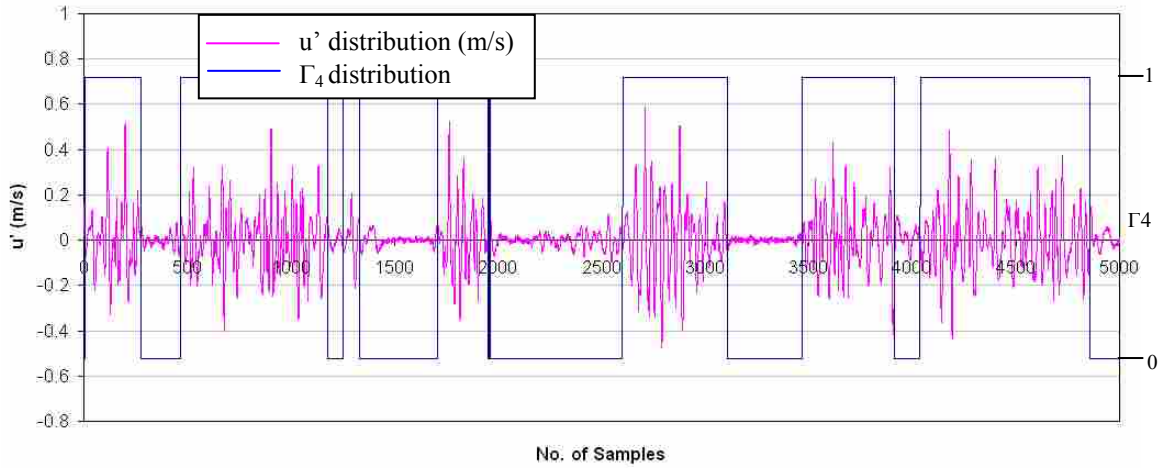

Figure 3-5: u' and Γ_4 distributions for an intermittency value of γ =0.68

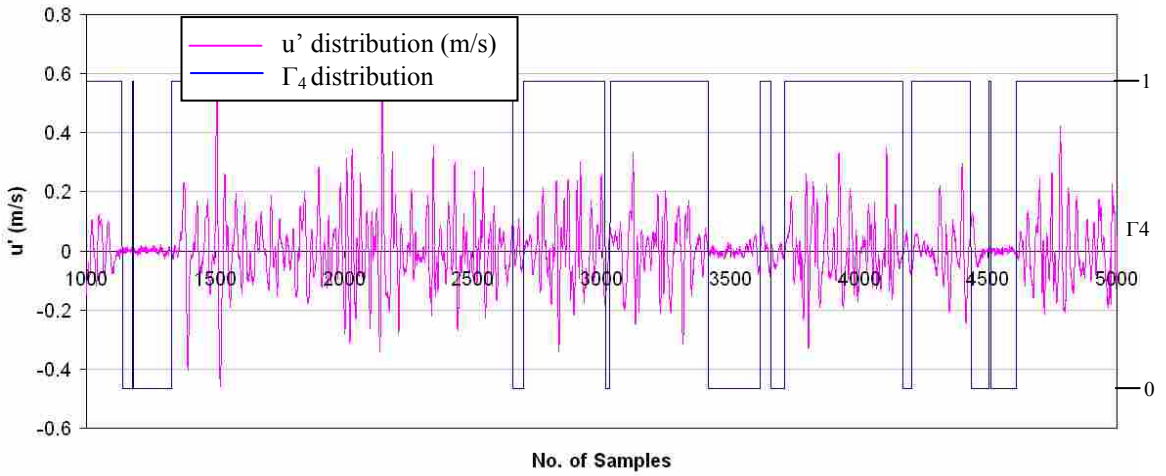

Figure 3-6: u' and Γ_4 distributions for an intermittency value of γ =0.86

3.3 Higher Order Turbulent Statistics vs. Intermittency Discriminator

Further validation of the intermittency detection routine was performed in the cascade. Data were taken using the blade follower device on the L1M profile for both steady (no control) and pulsing VGJ conditions at a single spanwise location. The data were taken near mid-span, two jet hole diameters above the top of a VGJ hole (negative z-direction). Mean velocity, fluctuating velocity, as well as skewness, kurtosis, kurtosis of the acceleration, and intermittency were measured and calculated. Figure 3-7 contains a plot of mean velocity normalized by the inlet velocity (u_{mean}/U_{in}) on the L1M blade at steady conditions. The data are presented as taken with respect to the blade as well as in wall-normalized axial chord coordinates where the x-axis is the axial chord location and the y-axis is the wall distance normalized by the axial chord. The remainder of hot-film data taken with the blade following device will be presented in the wall-normalized axial chord coordinates.

Figure 3-8 contains the no control hot-film measurements of u_{mean}/U_{in}, u_{rms}/U_{in}, skewness, kurtosis, kurtosis of the acceleration, and intermittency. The mean velocity plot u_{mean}/U_{in} of Figure 3-8(a) shows a clear separation near x/c_x=0.59. At this location a free shear layer forms and can be seen in the u_{rms}/U_{in} plot of Figure 3-8(b). The free shear layer begins to break down near x/c_x=0.7 and at a wall elevation of y/c_x=0.02 as the u_{rms}/U_{in} levels begin to rapidly rise above 20% and spread toward the wall. Along the initial path of the free shear layer and continuing away from the blade wall, the skewness plot shows a band of negative skewness values. This occurs due to predominately high velocity flow being punctuated by occasional bursts of low

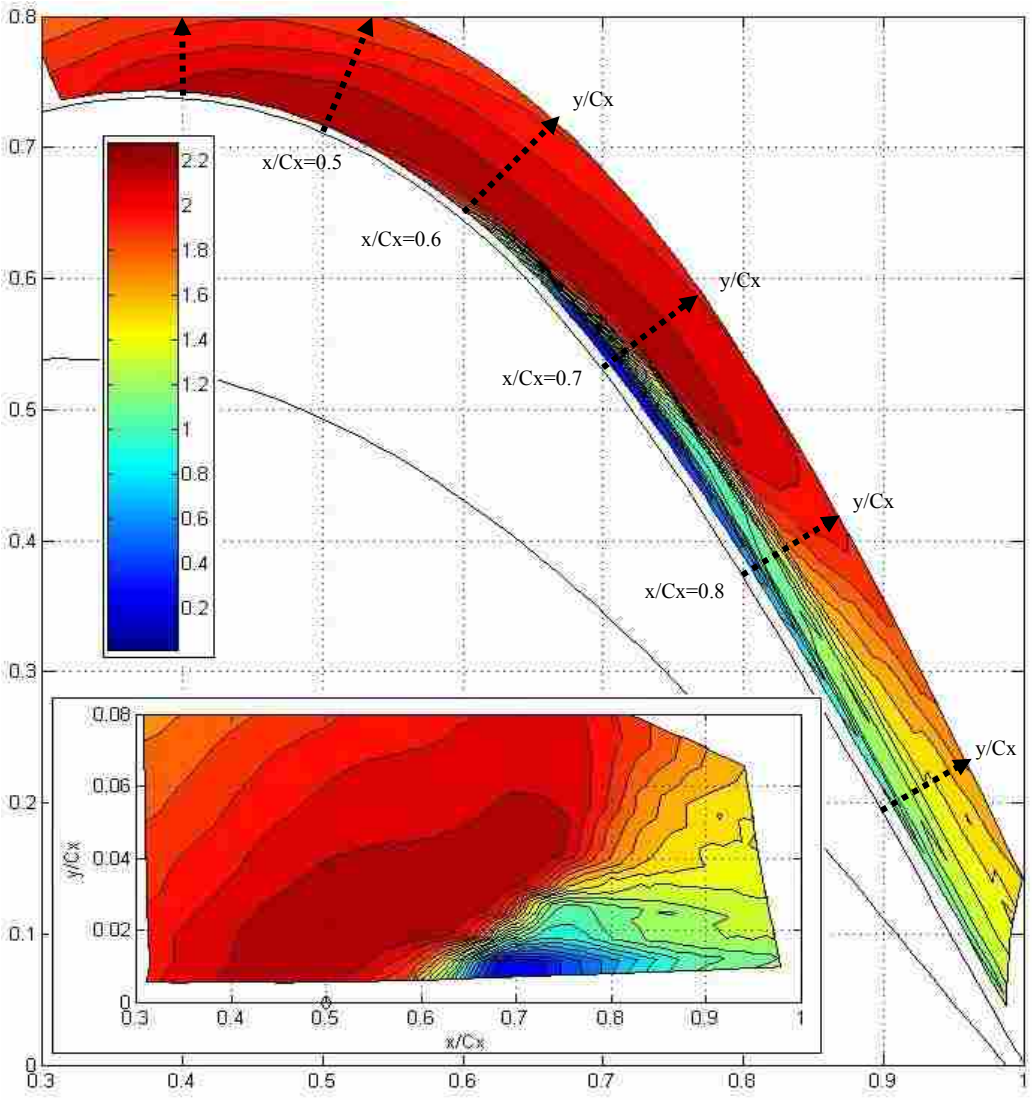

Figure 3-7: u_{mean}/U_{in} data for L1M with B = 0 presented in blade coordinates and in wall-normal axial chord coordinates

momentum fluid as depicted in the schematic in Figure 3-9. As the flow transitions to fully turbulent, the skewness values again return to zero. Cattanei [18] also made note of these negative values of skewness in regions of transitioning flow. Positive values of skewness occur in the separation region where the hot-film cannot distinguish reverse flow. Reverse flow is measured by the hot-film sensor as a positive u velocity, so any

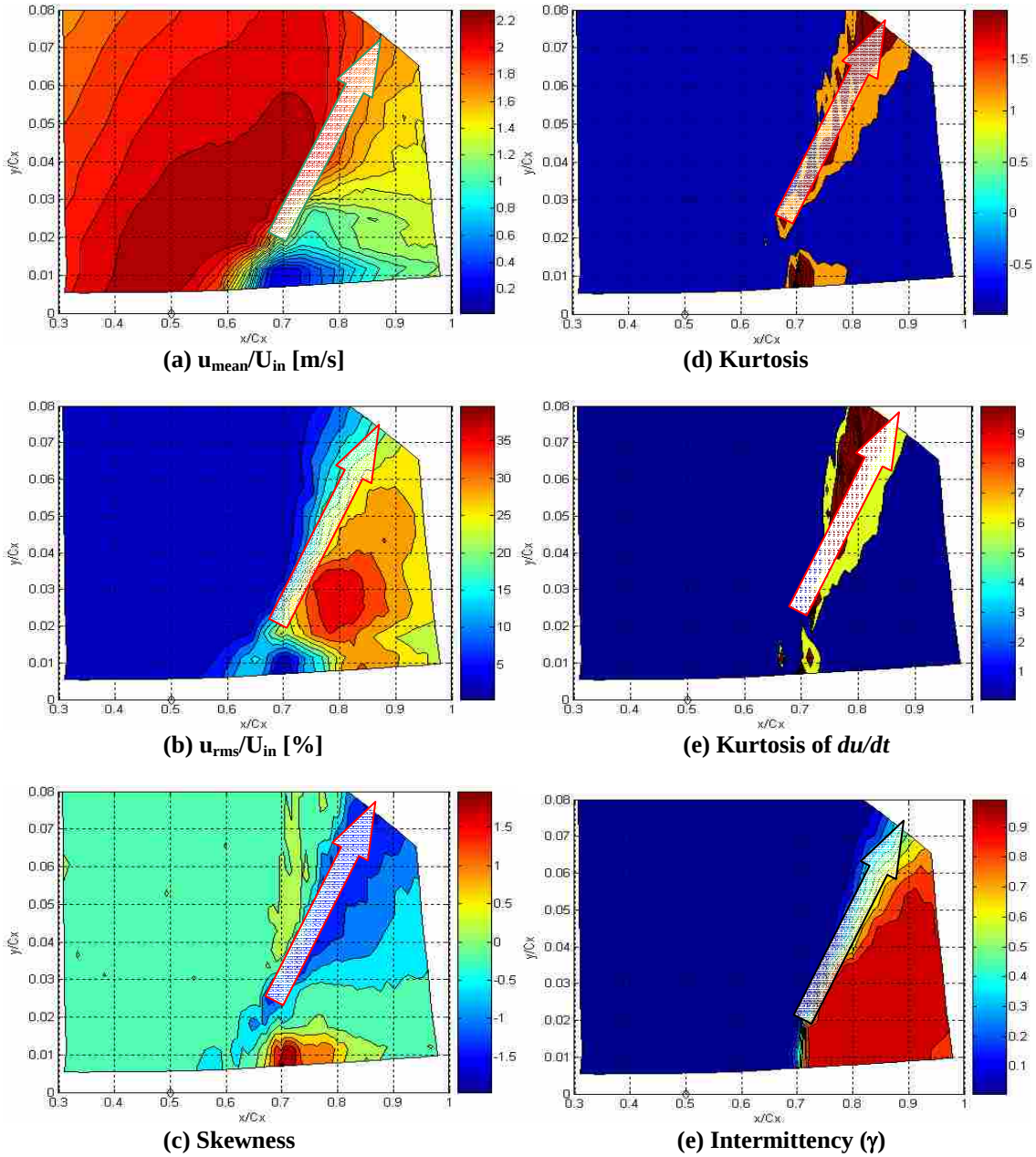

Figure 3-8: No control hot-film measurements on L1M for intermittency validation

unsteadiness in the separation bubble will result in positive velocity reading relative to the low velocity environment of the separation bubble. This is shown schematically in Figure 3-10. Both the kurtosis and kurtosis of the acceleration show elevated levels along the same location as the negative skewness, and start near the location of shear

layer breakdown in Figure 3-8(b). These indicative bands of transition continue into the freestream as displayed by the white arrows on each contour plot. The intermittency plot of Figure 3-8(e) shows a transition region where the levels of intermittency transition from 0 (fully laminar) to 1 (fully turbulent), which corresponds quite well with the location of the transition region indicated by the other statistical indicators. It should be noted that the y/c_x vs. x/c_x format of these color plots makes the transition appear more abrupt than actually occurs on the blade, as seen in Figure 3-11.

Figure 3-9: Signal of predominately high momentum fluid with occasional bursts of low momentum laminar flow resulting in negative skewness

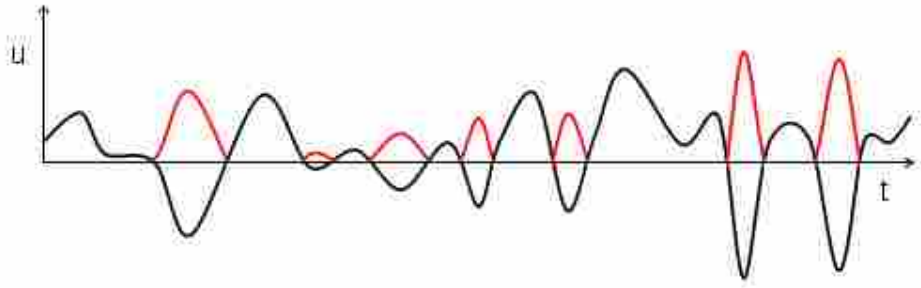

Figure 3-10: Negative velocities are measured as positive velocities by the hot-film sensor resulting in positive skewness

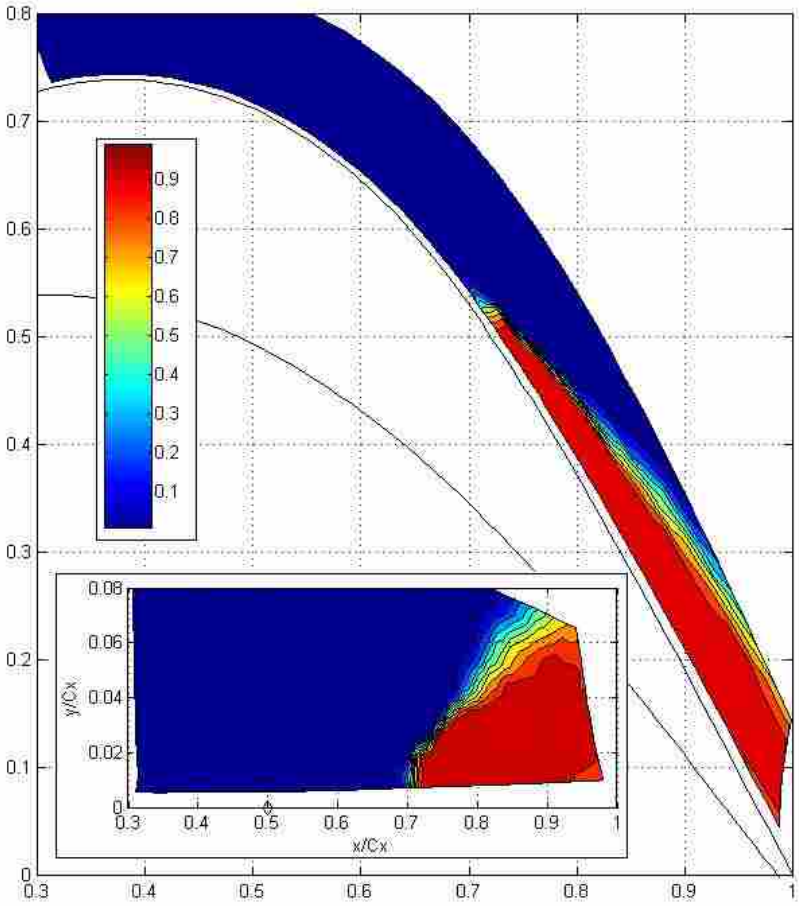

Figure 3-11: Intermittency plot in blade coordinates and normalized axial chord coordinates

For the unsteady pulsing VGJ data sets, intermittency is also compared to skewness and kurtosis of *du/dt*. Unfortunately, the kurtosis is not a useful transition indicator for this unsteady flow and will not be used further. Figure 3-12 contains 10 of the 24 phases from the VGJ pulsing cycle displaying intermittency, skewness, and kurtosis of *du/dt* on the L1M blade. The phase number is in the upper right hand corner of each plot. The first 5 rows of Figure 3-12 are during jet actuation indicated by black arrows, while the last 5 rows are after the jet has turned off. Throughout nearly every phase both the skewness and the kurtosis of *du/dt* show evidence of transition. The skewness plots contain bands of negative skewness often preceded by bands of positive

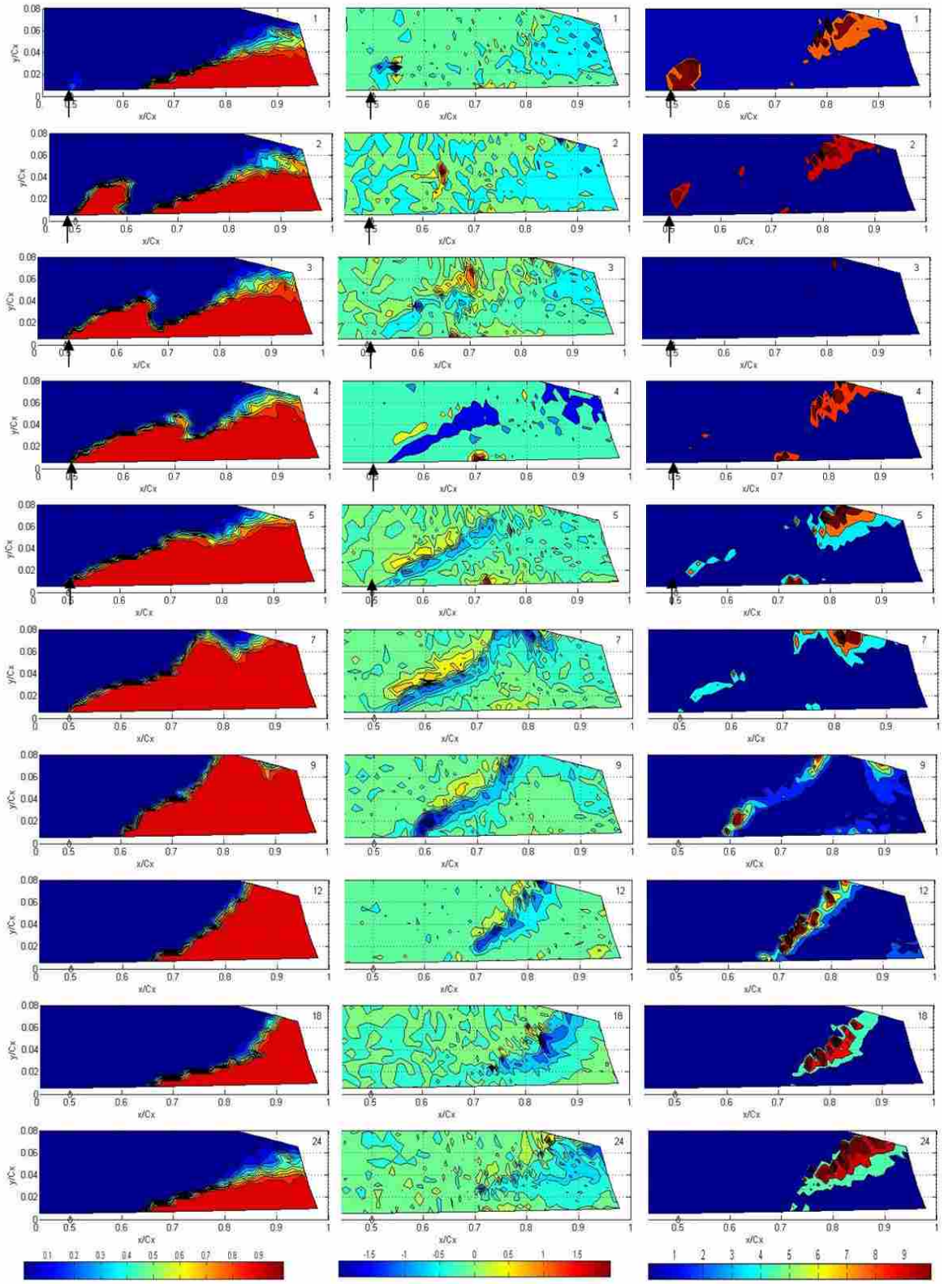

(a) Intermittency **(b) Skewness** **(c) Kurtosis of *du/dt***

Figure 3-12: Contour plots of various transitional indicators at 10 different phases in VGJ cycle on L1M

skewness which were not as apparent in the steady data. The positive skewness results from a velocity history of predominately low momentum fluid which is interrupted by occasional bursts of high momentum turbulent flow. A schematic of velocity histories with positive and negative skewness is displayed in Figure 3-13. The kurtosis of *du/dt* plots also contain distinct regions of elevated values throughout the VGJ cycle. Again, these regions of flow transition indicated by the skewness and kurtosis of *du/dt* correspond to the location of transition seen in the intermittency plots. Since the intermittency seems to agree so well with the transitional indicators of skewness and kurtosis of *du/dt* for both steady and unsteady conditions, and because it displays these transition regions so clearly, it will be used as the primary tool for transition investigations throughout the following chapters.

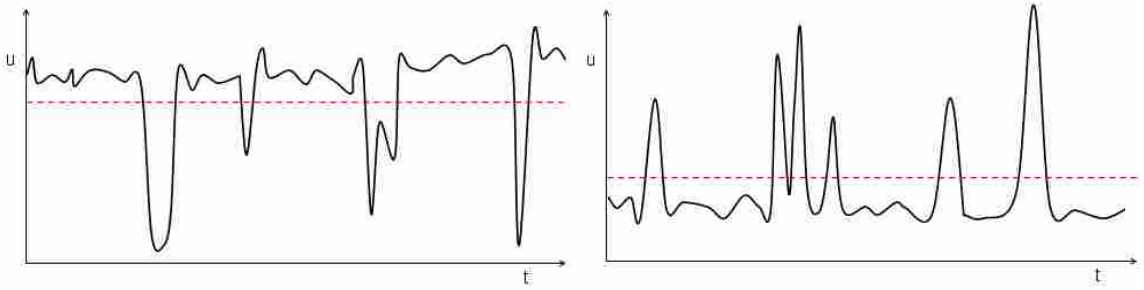

Figure 3-13: Schematic of (a) negative skewness and (b) positive skewness velocity signals

3.4 Intermittency Filter

As a transitional indicator the intermittency works very well, as supported by the other turbulence indicators discussed in the previous section. However, very near the wall as the mean velocity decreases in the boundary layer, the intermittency threshold (Γ_1) is decreased and the intermittency discriminator can predict transition too early. In addition, the data is processed and analyzed using Matlab which can have trouble

accurately representing high gradients on a color contour plot. As a result, laminar to turbulent transition, which usually occurs in a separated shear layer and then propagates to the wall, erroneously appears very near the wall. In order better represent real transitional behaviors, the intermittency plots are sometimes filtered such that all intermittency values below 0.97 are set to zero. Figure 3-14 depicts intermittency plots before and after filtering at one phase of an unsteady condition where laminar to turbulent transition naturally occurs in the separated shear layer. Figure 3-14(a) shows early transition prediction very near the wall due to the decreased velocity in the boundary layer. The point where the transition band begins to slope away from the wall corresponds well with the location of laminar separation of the shear layer. By filtering the intermittency plot it becomes apparent that transition is indeed beginning in the free shear layer and then spreads toward the wall as seen in Figure 3-14(b). Figure 3-15 contains the corresponding plot of u_{rms}/U_{in} showing increasing levels of unsteadiness starting in the shear layer and spreading toward the wall. This can be directly compared to the filtered intermittency plot of Figure 3-14(b). Even though the filtered intermittency plot does not depict the onset of transition, it does show the shear layer breakdown behavior which is not seen in the unfiltered plot. Throughout the remaining chapters, filtered intermittency plots will often be used for unsteady cases in order to highlight transitional behaviors rather than locate the onset of transition. Unfiltered intermittency plots will be used when transition location is discussed and when the purpose is not to show the shear layer breakdown.

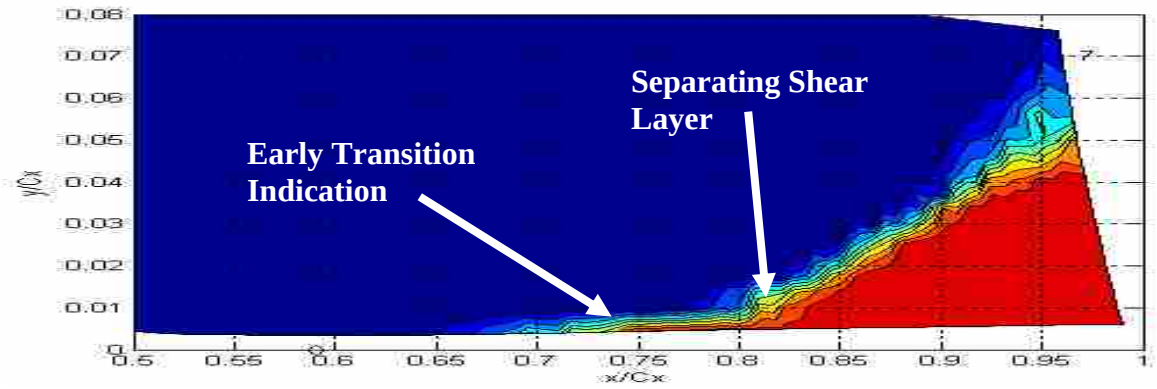

(a) Intermittency without filtering

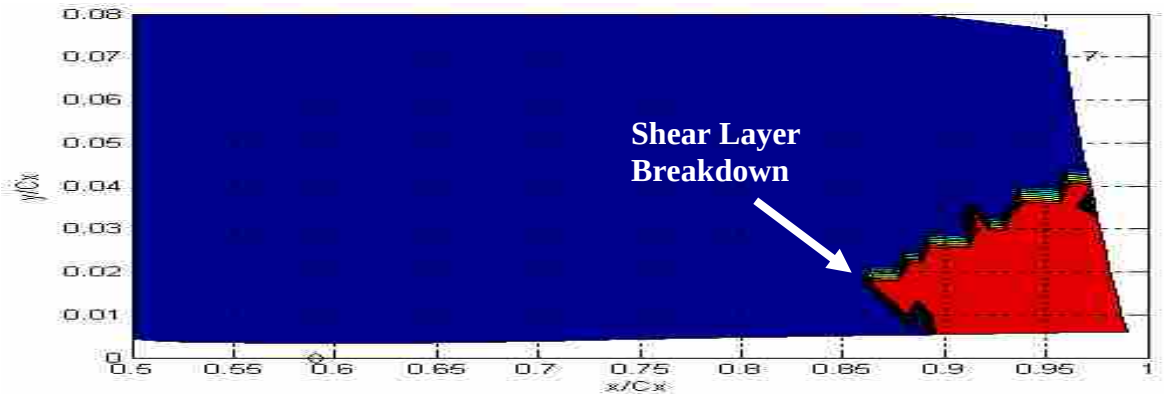

(b) Intermittency with filtering at 0.97

Figure 3-14: Unfiltered and filtered intermittency contour plots

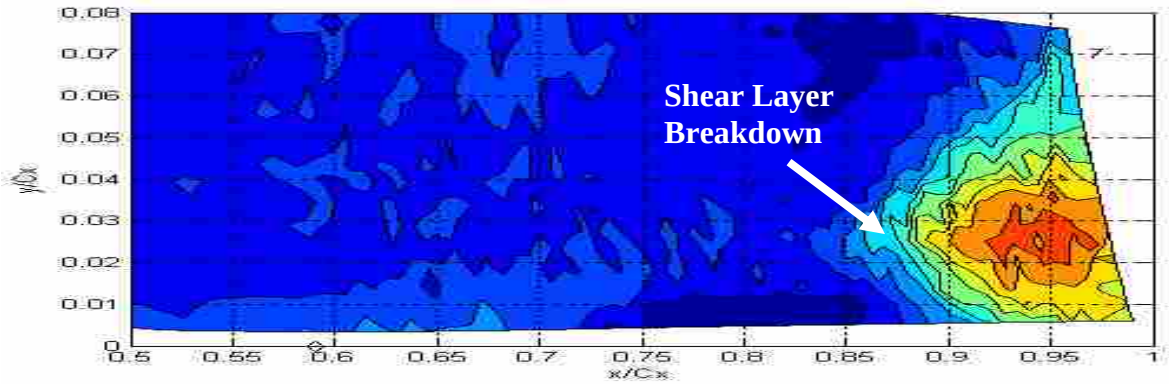

Figure 3-15: u_{rms}/U_{in} showing shear layer breakdown corresponding to filtered intermittency plot

4 Blade Comparison – Pack B and L1M

A direct comparison is made between two different LPT profiles, the Pratt and Whitney Pack B research blade and an Air Force developed L1M blade. The Pack B is a aft-loaded blade which exhibits a separating, non-reattaching separation bubble, while the L1M is a mid-loaded blade with a separating, reattaching separation bubble. The purpose of this comparison is to study the effects of VGJs on two different types of separation bubbles and to examine which LPT profile is a better candidate for flow control.

The experimental pressure coefficient (c_p) distributions are presented in Figure 4-1 and Figure 4-2 for the L1M and the Pack B respectively. Figure 4-1 also contains a MISES prediction with and without separation (high and low Re) from Bons et al. [23]. In the low Re MISES prediction, forced transition as specified by the Praisner and Clark transition model produced reattachment just before the blade trailing edge [25]. Uncertainties in the experimental pressure measurements translate to an uncertainty of ±0.10 in the c_p data at Re_c = 20,000. For the L1M, the predicted separation zone is broader than that obtained experimentally, suggesting that the experimental transition location is earlier than expected. This is possibly due to the lower inlet turbulence level (0.5%) used in the calculation compared to the experiment (3%). Of significant note for this study is that the c_p data indicate reattached flow by 84% c_x, suggesting a closed separation bubble. With flow control, the c_p profile has a reduced separation zone and

follows closely the non-separating MISES calculation, particularly in the diffusing region of the blade (50-90% c_x). From this it is clear that the pulsed VGJs are effective in the time-average sense at reducing laminar separation.

In addition to the experimental data, Figure 4-2 includes a non-separating VBI CFD prediction for the Pack B from Sondergaard et al. [26]. The aft-loading of the Pack B is immediately evident in the later peak c_p location (63% c_x vs. 47% for the L1M). c_p data are presented for both high and low Reynolds numbers without control as well as for low Re with flow control. Trailing edge boundary layer separation is evident in the low Reynolds number (no control) case, with the last pressure tap at 90% c_x still indicating separated flow. The effect of this larger, non-reattaching separation bubble is evident well upstream of the peak c_p location as shown by the reduced c_p values compared to the high Re_c case. Again, in the case with flow control, the separation is reduced and the blade performance improves markedly, indicating attached flow in a time-averaged sense.

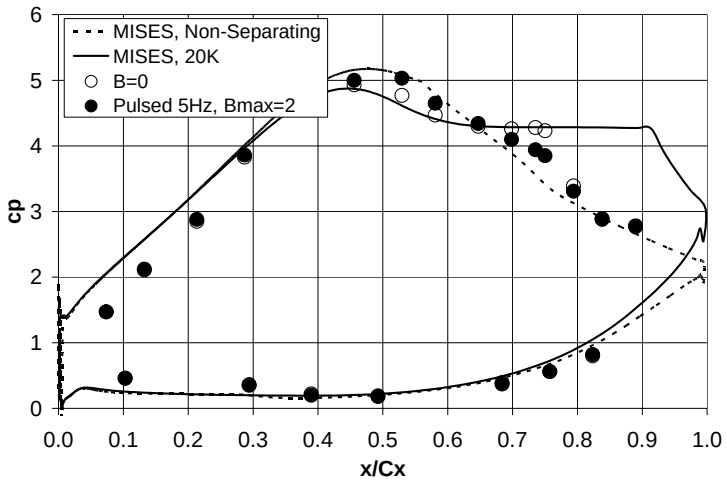

Figure 4-1: c_p distributions for L1M at B=0 and B_{max}=2.1 (5Hz) at Re_c=20K vs. MISES prediction

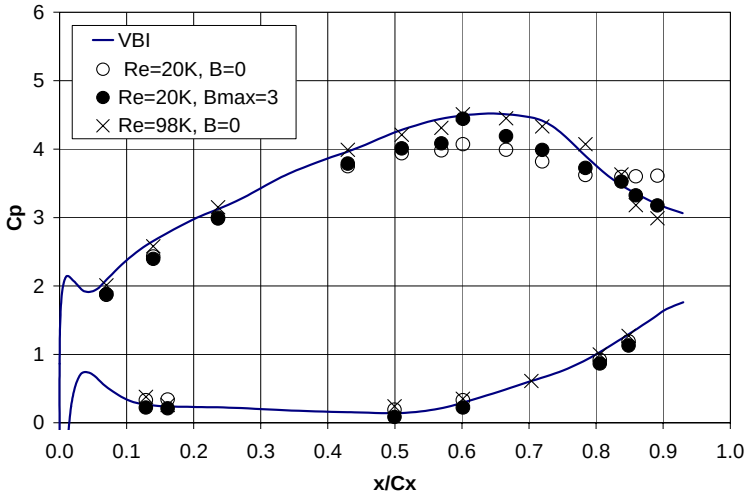

Figure 4-2: c_p distributions for Pack B at B=0 and B_{max}=1.8 (5Hz) at Re_c=20K & B=0 at Re_c = 98,000 vs. VBI prediction

4.1 No Control

Figure 4-3 shows the uncontrolled data for both the L1M and the Pack B cases. Figures 4-3(a)-(f) include plots of: u_{mean}/U_{in}, u_{rms}/U_{in}, skewness, kurtosis, kurtosis of the acceleration, and the intermittency. The first difference that can be seen in Figure 4-3(a) is that the maximum velocity is well into the near wall region of the L1M blade but is removed from the wall in the Pack B case (maximum u_{mean}/U_{in} locations are indicated on both plots). This more significant upstream influence of the separation zone in the Pack B data corroborates the c_p profile data shown earlier in Figure 4-3(b). In the absence of a wall shear measurement to precisely identify the separation location, it was determined from Figures 4-3(a) and (b) that the separation location for the L1M blade is near 59% c_x, while separation occurs near 68% c_x for the Pack B. This is identified in the plots by the region of rising near wall u_{rms} accompanied by a sharp drop-off in u_{mean} that occurs as the boundary layer becomes a separated free shear layer. (Incidentally, both of these

separation locations are approximately 9% c_x downstream of the VGJ location for the respective blade design. Thus, the convective distance between the control point and the uncontrolled separation inception location is roughly equivalent in both cases.) Following separation, the region of rising turbulence lifts away from the wall and forms a separated free shear layer above a region of unsteady reverse near-wall fluid. After a short distance, this laminar free shear layer begins to transition to a turbulent shear layer. The subsequent turbulent breakdown then spreads rapidly toward the wall in both cases. As identified on the plots, the separated shear layer from the L1M begins turbulent breakdown near 70% c_x while breakdown occurs around 84% c_x for the Pack B. Based on these results, the laminar free shear layer extent is 11% c_x for the L1M (59% c_x separation to 70% c_x transition) and 16% c_x for the Pack B (68% c_x separation to 84% transition). The decreased transition length in the L1M case is likely due to the more aggressive deceleration of the mean flow noted in the c_p profile, given that adverse pressure gradients are known to be destabilizing. The peak level of turbulence in the turbulent shear layer reaches down to the nearest wall measurement location by 82% c_x for the L1M profile (as indicated in the plot), while the maximum turbulence level never penetrates down to the blade surface for the Pack B. It is thus concluded that the separated region successfully reattaches for the L1M around 82% c_x while the Pack B separation does not fully reattach in the measurement domain.

Regions of unsteady reverse flow can be detected as areas of positive skewness in the near wall region of Figure 4-3(c). Because the hot-film is only sensitive to velocity magnitude, any negative (reverse flow) velocities are positively justified resulting in positive skewness values in regions of low or near-zero u_{mean}. Both the L1M and Pack B

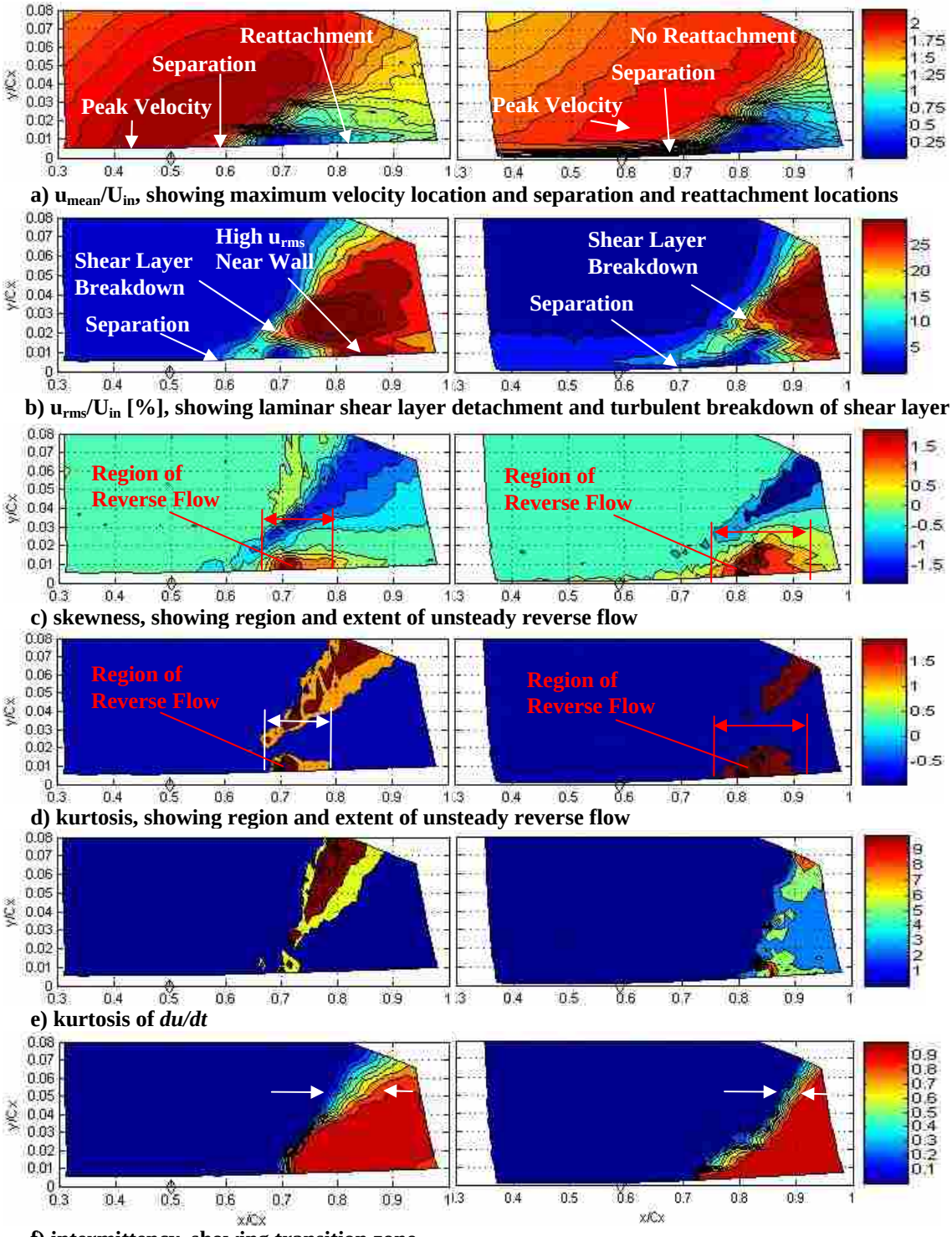

a) u_{mean}/U_{in}, showing maximum velocity location and separation and reattachment locations

b) u_{rms}/U_{in} [%], showing laminar shear layer detachment and turbulent breakdown of shear layer

c) skewness, showing region and extent of unsteady reverse flow

d) kurtosis, showing region and extent of unsteady reverse flow

e) kurtosis of *du/dt*

f) intermittency, showing transition zone

L1M **Pack B**

Figure 4-3: No control (B=0) at Re_c=20,000. a) u_{mean}/U_{in}, b) u_{rms}/U_{in} [%], c) skewness, d) kurtosis, e) kurtosis of *du/dt*, and f) intermittency

show regions of strong positive skewness beneath the separated free shear layer. The streamwise extent of this unsteady reverse-flow region is about 70% longer in the Pack B case compared to the L1M. Because the flow turning is not yet complete at this blade location, the extended streamwise bubble length causes the Pack B free shear layer to migrate further from the blade surface before breakdown (nearly 50% further than the L1M). As the shear layer reattaches to the blade, the skewness returns to zero values near the wall for the L1M profile. The same is not true for the Pack B data, again emphasizing that the Pack B boundary layer never fully reattaches within the data domain. This same region of reversed flow in the heart of the separation region also shows elevated levels of kurtosis (Figure 4-3(d)).

Following the trajectory of the separating free shear layer and continuing out into the freestream are bands of strongly negative skewness as seen in Figure 4-3(c). These regions are indicative of high velocity flow punctuated by short bursts from lower momentum laminar pockets. The higher order kurtosis and the kurtosis of acceleration show elevated readings along the same location as the vicinity of negative skewness. As expected, these transition indicators suggest the location of transition occurs in the region of the shear layer breakdown as mentioned above and indicated in the plots (i.e. shear layer transition at $x/c_x = 0.7$and $y/c_x = 0.02$ on the L1M and at $x/c_x = 0.84$ and $y/c_x = 0.03$ on the Pack B). It is interesting to note that the width of the skewness, kurtosis, and the kurtosis of the acceleration bands is much larger in the L1M plots than for the Pack B, particularly in the freestream. This indicates that the flow is transitioning over a longer streamwise distance for the L1M than for the Pack B. Since the Pack B shear layer is further from the wall when it finally transitions, the evolution to a fully turbulent

character is perhaps less influenced by the proximity of the wall. Thus even though the Pack B laminar shear layer convects further downstream before beginning to transition, it appears to transition more rapidly. The intermittency indicator plotted in Figure 4-3(f) agrees well with the transition location suggested by plots (c), (d), and (e).

4.2 Pulsed Jets

The unsteady follower data with pulsed VGJs is presented for only one spanwise location (approximately two jet diameters above the upper lip of a VGJ hole near the blade midspan). Since the jet injection direction is upwards along the span, the data plane is in the direct path of the jet injection (only two jet diameters away from the injection point). Accordingly, the jet event figures prominently in the data presented herein. The schematic above the plots in Figure 4-4 indicates the locations of the 24 phases used to analyze the unsteady data. Figure 4-4 shows a series of ensemble averaged $\tilde{u}/U_{in}$ contour plots for the 12 even-numbered phases for both the L1M and Pack B data.

As in the uncontrolled case (Figure 4-3), ensemble averaged peak velocities in Figure 4-4 penetrate down closer to the wall for the L1M blade than they do for the Pack B. For both cases, the jet pulse causes an initial bunching up of the separation region followed by its eventual ejection off the back of the blade. This evolution of the perturbed separation bubble is summarized in Figure 4-5 using the ensemble average velocity data in Figure 4-4. Figure 4-5(a) shows the upstream and downstream extent of the separation bubble in the axial chord direction as a function of phase for each blade profile. The L1M bubble data is shaded blue between the furthest upstream and

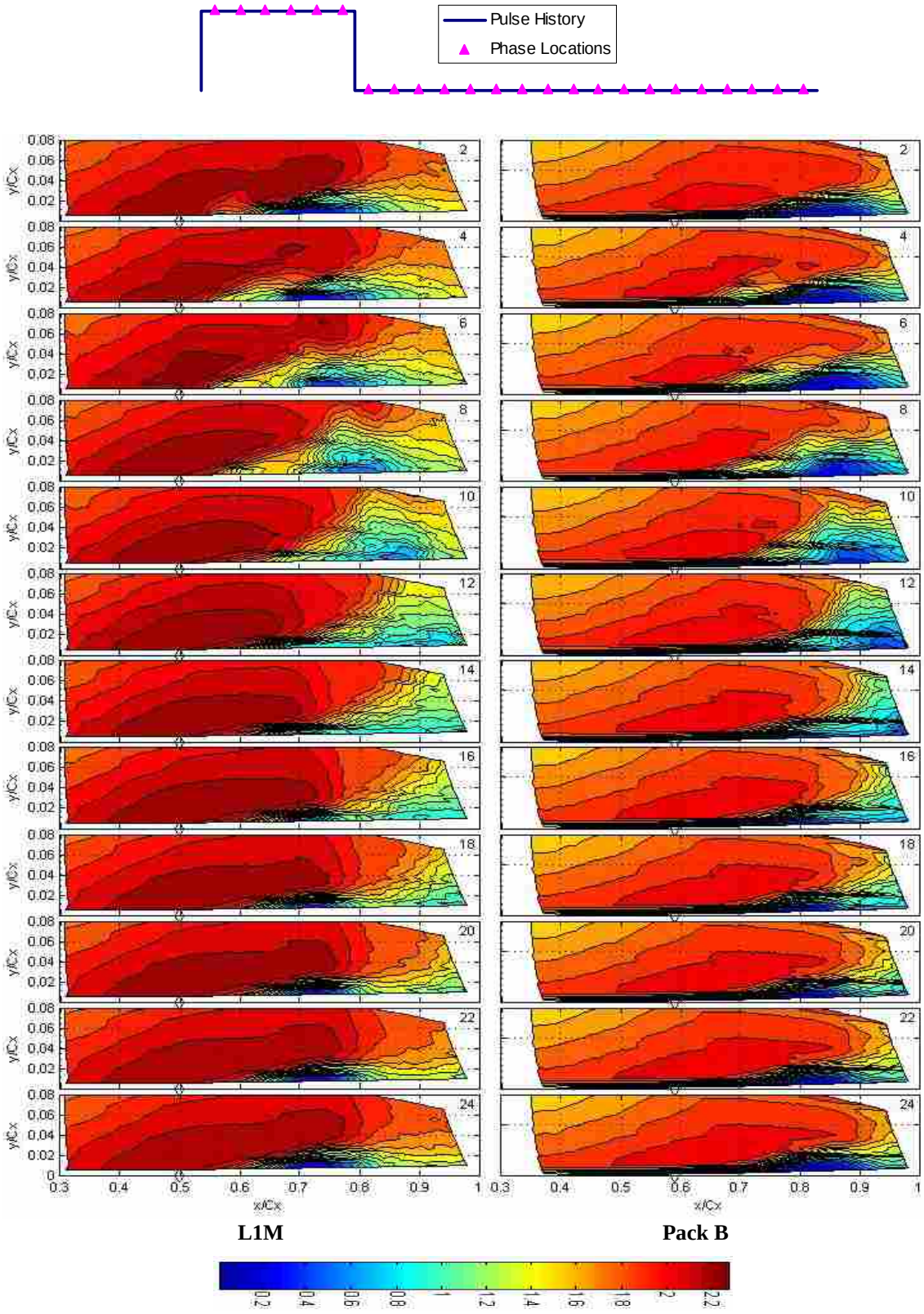

Figure 4-4: u_{mean}/U_{in} plots for L1M (left) and Pack B (right). Pulsed blowing at 5Hz with $B_{max} \cong 2$. Even phases 2-24

downstream extents, while the Pack B bubble data is shaded yellow. For purposes of this plot, the separation zone is defined as any region of the flow with less than 40% of the peak velocity in the measurement domain. The pulse history is shown along the bottom of the plot so that the response of the separation bubble can be tied directly to the control initiation and termination events. Essentially, the VGJ pulse causes a disturbance at the leading edge of the bubble which ultimately pushes the separation region off the back of the blade. In both cases, some residual separated flow remains on the blade after the bulk of the bubble is ejected, and this residual grows to form a new separation bubble until it is impacted by the next jet pulse. As seen in Figure 4-5(a), the mean trajectory of the L1M bubble displacement is steeper during its migration off the back of the blade. This is due to the higher freestream velocity present in the L1M passage that is sweeping the low-momentum fluid with it off the blade. After the separation bubble gets pushed off the back of the blade, the residual separation centered near 71% c_x continues to grow until the next jet pulse arrives. The Pack B bubble responds more slowly to the jet pulse, due to the reduced convective velocity of the jet disturbance and the larger separation bubble at the time of jet impact. Once the separation zone has been swept off the blade, new separation growth is centered around 82% c_x, expanding quickly to its former streamwise extent. In both cases, the streamwise extent of the bubble decreases in response to the injected jet since the upstream end is effected before the downstream end. Thus, the bubble bunches up, becoming thicker in the blade-normal direction, before being convected off the blade.

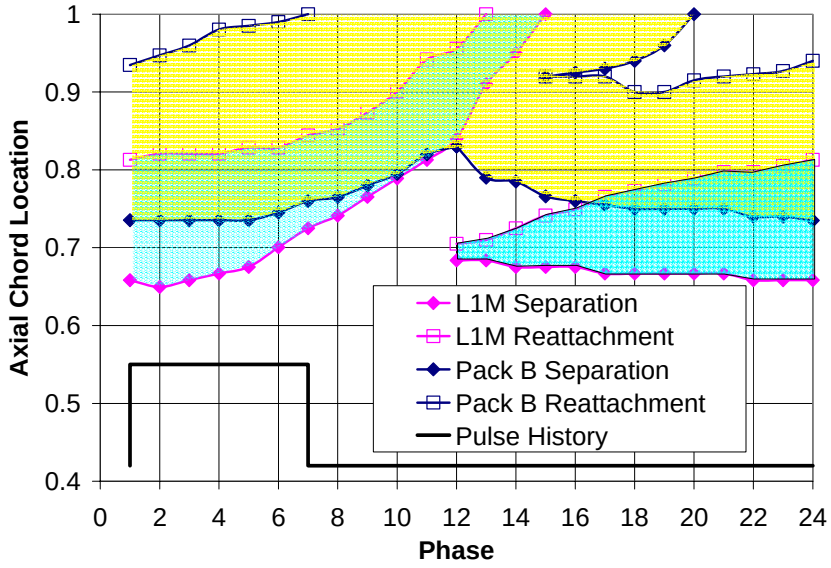

a) separation bubble maximum upstream and downstream extent

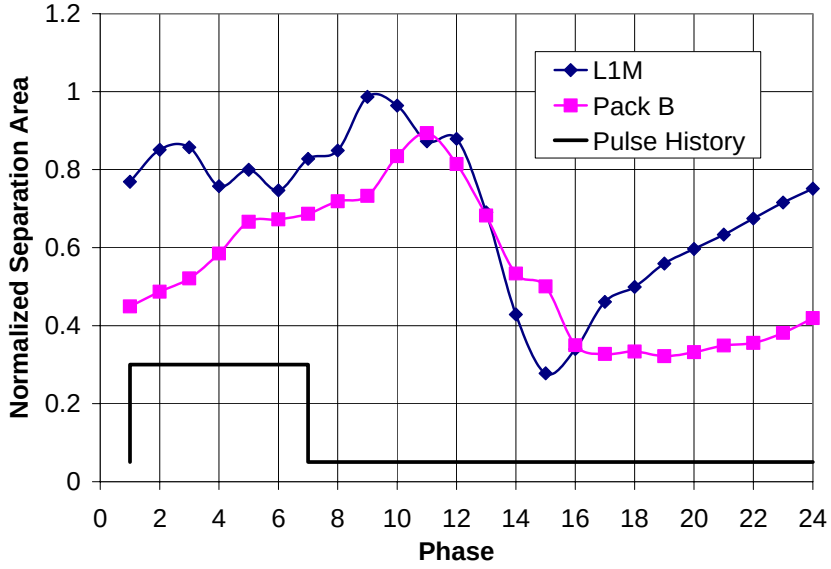

b) integrated separation bubble area normalized by bubble size with no control (B = 0)

Figure 4-5: Separation bubble evolution (defined as region where $\tilde{u} < 0.4\tilde{u}_{\max}$ in Figure 4-4)

While Figure 4-5(a) provides a measurement of the maximum streamwise extent of the separation zone, it is apparent from Figure 4-4 that the low momentum regions on the two blades have different wall-normal "thicknesses" as well. For instance, though the bubble regrowth (phases 16-24) on the Pack B has a longer streamwise extent than the

L1M, it is much thinner and thus contains less stagnant fluid. One way to characterize this change in separation bubble shape is to integrate the low-momentum area as a function of phase (Figure 4-5(b)). In this plot, the integrated separation size is normalized by the separation bubble size without control (B=0) for both the L1M and Pack B cases. Thus, a normalized separation area of unity represents no change in bubble size from the no-control baseline case. As in Figure 4-5(a), the separation zone is defined as the region of the flow with less than 40% of the peak velocity. An initial observation from Figure 4-5(b) is the overall level of control offered by VGJs for the different cases. The average reduction in separation area for the Pack B is roughly 50%, whereas the L1M data hovers around 0.85 (only 15% net reduction) for over half of the pulsing cycle. Since the uncontrolled separation is 2.5 times larger in area on the Pack B than on the L1M, the controlled L1M data still has less separation area; however, the percent reduction in area due to flow control is significantly less than the Pack B. In order to interpret the trends in Figure 4-5(b), it must be remembered that the L1M separation bubble is centered much further upstream from the trailing edge than the Pack B separation. Consequently, during phases 1-6 the L1M separation is being convected downstream without any significant change in size. From phases 6-10, the L1M separation bunches up as indicated earlier producing a sharp increase in size (even reaching the no control size at one point). After phase 12, the rounded separation zone begins to convect out of the measurement domain and off the blade, thus the precipitous drop in separation size. The minimum reduction in size is approximately 70%. Following this, the bubble regrowth is approximately linear until phase 2, just before the next pulse impacts the bubble leading edge.

The Pack B data show a very different bubble response in Figure 4-5(b). First, when the jet is turned on, the bubble size is still growing unimpeded. By phase 6 the effect of the jet becomes evident as the bubble growth slows somewhat. This slower response was noted in Figure 4-5(a) and is due to the slower convection speeds in the Pack B cascade. The bubble grows to within 90% of its no-control size before exhibiting a monotonic decrease from phases 11 to 16. The bubble reduction is more gradual compared to the L1M case, though it eventually reaches the same minimum point (~ 0.3) at roughly the same phase. Following this, there is a lagged response from phase 16 to 22 wherein the bubble size does not change. Not until phase 23 does the linear growth rate begin with roughly the same slope as the L1M. The growth continues until the effect of the next pulse becomes apparent again in phase 6. This lagged response from phases 16-22 is a characteristic noted previously by Bons et al., and is clearly not a characteristic of reattaching separation bubbles (e.g. the L1M) [6]. Apparently, the large amplitude flow oscillations associated with the ejection of a non-reattaching separation bubble create a temporary flow inertia that maintains the attached state for some finite period of time (50ms in this case) after the separation has been eliminated and the control is off.

The unsteady jet interaction with the separation bubble can also be viewed in a time-space plot (Figure 4-6). A similar presentation was used by Volino et al. for their synthetic jet data [7]. This figure shows the ensemble averaged turbulence and intermittency over two jet cycles at a constant wall distance for both blade configurations ($y/c_x \cong 0.033$ for the L1M and $y/c_x \cong 0.036$ for the Pack B). Recall that in this case u_{rms} is the unsteadiness that remains after the bulk unsteady motion ($\tilde{u}$) corresponding to the 5Hz pulsing of the jets has been removed (see Figure 2-5). The trajectory of the jet

initiation is noted (with white arrows) as the lower edge of the elevated turbulence and intermittency band emanating from the jet hole at 50% c_x (for the L1M) and 59% c_x (for the Pack B). The average convection velocity of the jet disturbance is roughly 70% of the local freestream velocity for the L1M case and 85% for the Pack B. The distance required for the jet to penetrate from the wall to the elevation shown in the figures is approximately 15% c_x in both cases. The jet termination event convects at approximately the same velocity until it is engulfed in the separation bubble dynamics near the uncontrolled (B=0) transition location (highlighted with a vertical yellow band).

In the L1M case, the termination event merges with a very active separation zone at $x/c_x = 0.74$ and $t/T = 0.4$. After this the line of transition (and elevated u_{rms}) decelerates to roughly 20% of the average local velocity (indicated by the arrow). This deceleration occurs as the separation bubble is being pushed off the blade and the residual bubble is being thinned until it almost disappears from this y/c_x level by $t/T = 0.75$. Between $t/T = 0.75$ and 0.85 there is a brief lull in turbulent activity that bears some resemblance to the "calmed zones" following convected wake disturbances noted by Gostelow and Thomas, and Stieger and Hodson (noted on plot with red oval) [14, 27]. The calmed zone is typically marked by low turbulence levels and laminar-like boundary layer behavior. Following this, a resurgence of the separation bubble redirects the transition line back upstream to the uncontrolled (B=0) transition location at approximately the same velocity. The Pack B time-space plots show a similar behavior, though the calmed region is larger due to the phase lag in bubble regrowth as noted in Figure 4-5(b).

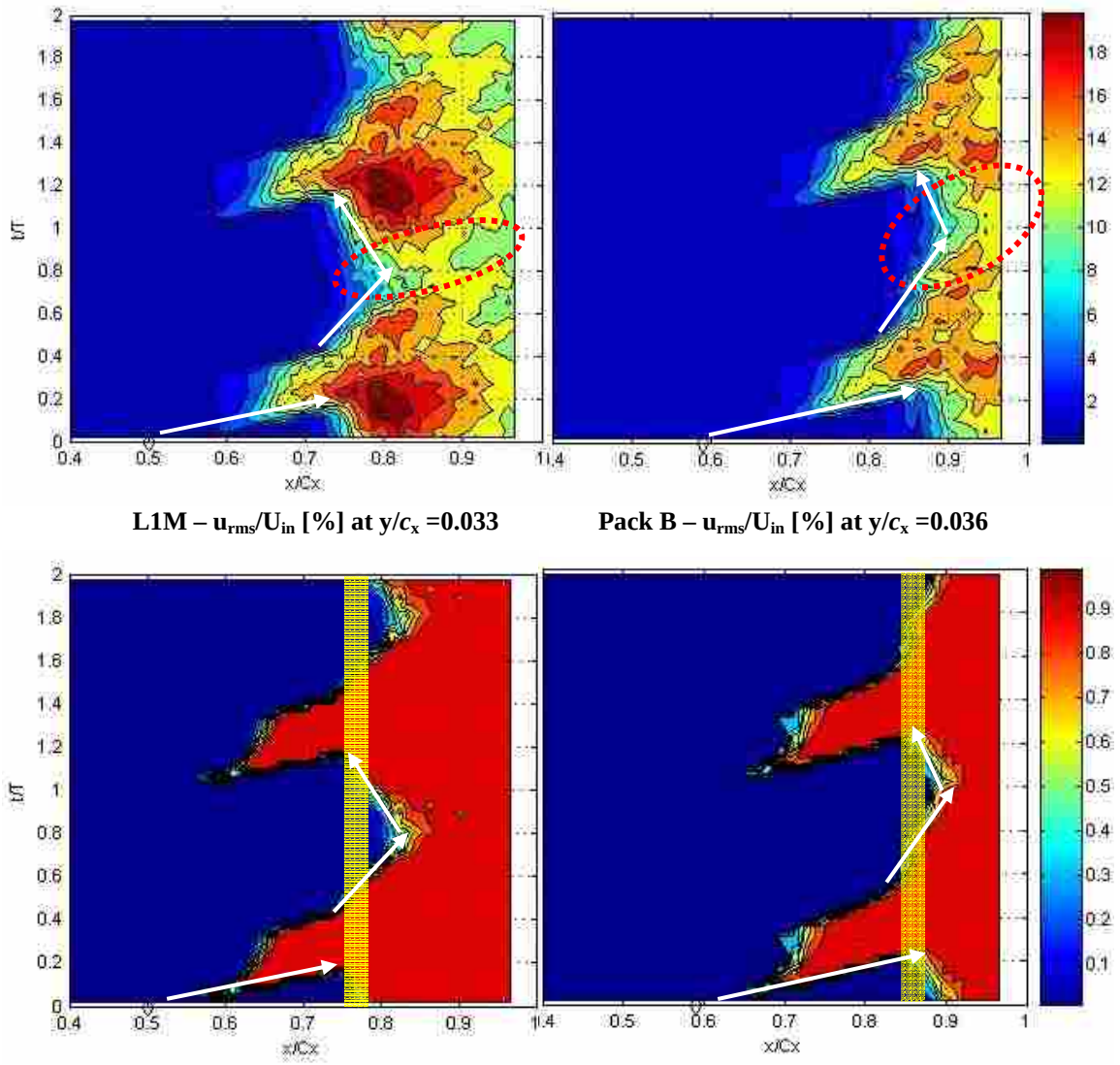

L1M – u_{rms}/U_{in} [%] at y/c_x =0.033 **Pack B – u_{rms}/U_{in} [%] at y/c_x =0.036**

L1M – intermittency at y/c_x =0.033 **Pack B – intermittency at y/c_x =0.036**

Figure 4-6: u_{rms}/U_{in} and intermittency time-space plots for L1M and Pack B. Yellow vertical band indicates transition location without control (B=0) at this y/c_x elevation [see Figure 4-3(f)]

A more complete picture of the transition dynamics can be made with the aid of the phase-locked intermittency plots of Figure 4-7. This figure shows the intermittency characteristics of the flow for both blade profiles at phases 2, 5, and 12. At phase 2 the jet has just been initiated and its influence on the local flow transition can clearly be seen. This region of transitioned flow is convected downstream at a higher velocity on the L1M blade, thus by phase 5 it has already combined with the downstream region of separation-

induced transition. For the Pack B, the jet-induced transition has not yet completely merged with the downstream region of transition by phase 5. After the jets are turned off, the transition migrates downstream. Just as the separation bubble bunches up before it is ejected, the line of transition also appears to bunch up as seen by the steeper slope of the transition region in phase 12 of Figure 4-7. After the separation region is ejected off the back of the blade the slope of the transition line again decreases prior to the initiation of the next pulse. As with the uncontrolled data in Figure 4-3, higher-order turbulence statistics can be used to corroborate the trends highlighted in the intermittency plots. Figure 4-8 and Figure 4-9 show skewness and kurtosis plots at phases 5 and 12 respectively for direct comparison with Figure 4-7. The regions of negative skewness in Figure 4-8 line up with the regions of transition indicated by the phase 5 intermittency plots. A single band of negative skewness identifies the merged jet and separation induced transition lines for the L1M while the two discrete bands of negative skewness for the Pack B indicate that the full impact of the jet influence has not yet reached the downstream region of transition. Also, the kurtosis plots at phase 12 (Figure 4-9) show the steeper transition line slope highlighted previously in Figure 4-7.

In conclusion, separation control for the L1M showed significantly less benefit (in terms of bubble size reduction) due to the upstream location of the bubble. Once the bubble was swept off, separation regrowth began immediately, and grew until the jet pulsing cycle restarted. For the Pack B blade, bubble regrowth was not evident for nearly 35% of the pulsing cycle after the separation bubble had been convected off the blade. Because of its larger separation and greater separation reduction in the presence of VGJs, the Pack B is a much better candidate for active flow control than the L1M.

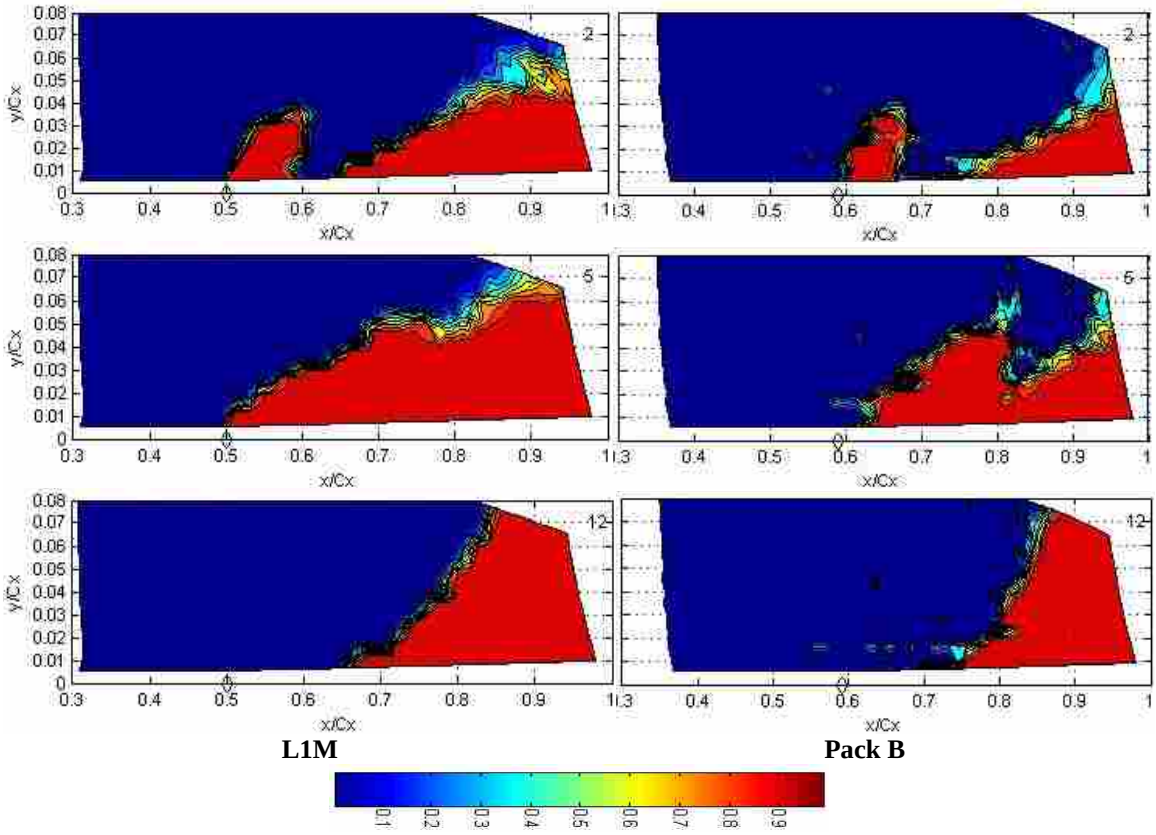

Figure 4-7: Intermittency plots for L1M (left) and Pack B (right) at phases 2, 5, and 12

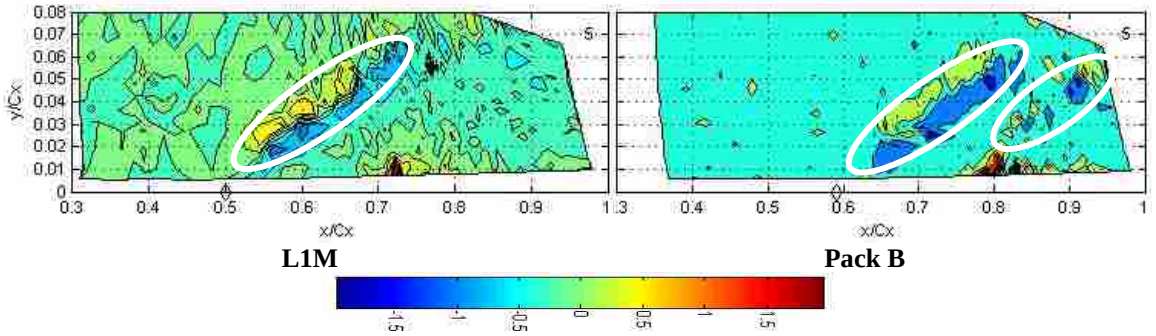

Figure 4-8: Skewness plots for L1M (left) and Pack B (right) at phase 5. Transition regions of positive/negative skewness identified by ovals

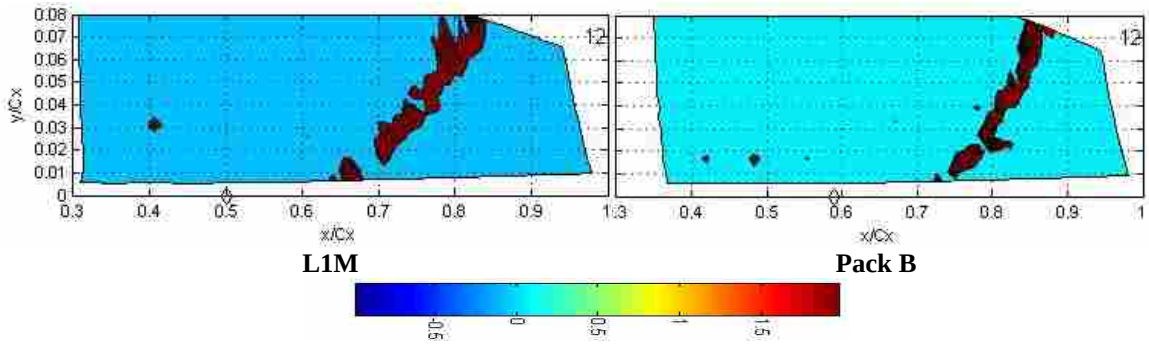

Figure 4-9: Kurtosis plots for L1M (left) and Pack B (right) at phase 12

5 Spanwise vs. Discrete Disturbances on Pack B

The L1M has a much smaller separation region, even though it has higher loading. This is primarily because the separation bubble separates earlier, resulting in earlier laminar to turbulent transition of the separated shear layer. This earlier turbulent breakdown of the separated shear layer allows boundary layer reattachment onto the aft portion of the L1M blade. The Pack B, due to its aft-loading, has a later separation. Although the separated shear layer does transition to turbulent on the Pack B, it happens later and does not result in the reattachment of the boundary layer. The Pack B not only has a larger separation region than the L1M, but the Pack B also sees a much larger decrease in separation size due to the presence of VGJs. End-wall losses are also likely to be larger on a mid-loaded blade like the L1M, making it less desirable for designers. For these reasons the Pack B is a much better candidate for VGJ implementation. Further studies were therefore made on the Pack B to compare the influence of unsteady wakes caused by the previous blade row in an engine and pulsing VGJs on the separation bubble.

5.1 Wakes vs. Pulsed VGJs

The pressure coefficient (c_p) distributions for the Pack-B blade pressure and suction surfaces are presented in Figure 5-1. The figure includes experimental data for

the uncontrolled case, for the presence of wakes, and for the controlled case with pulsed jets all at Re_c=20,000. It can be seen that for the baseline uncontrolled case the c_p values plateau by 80% axial chord which is indicative of boundary layer separation. In the presence of unsteady wakes the c_p values deviate from the inviscid prediction due to the lower Reynolds number but do not plateau as the uncontrolled case does. The c_p data with the pulsing jet follow very closely the uncontrolled c_p distribution until 80% axial chord when the pulsing jet c_p values drop down near the VBI prediction indicating a reattachment of the separated region.

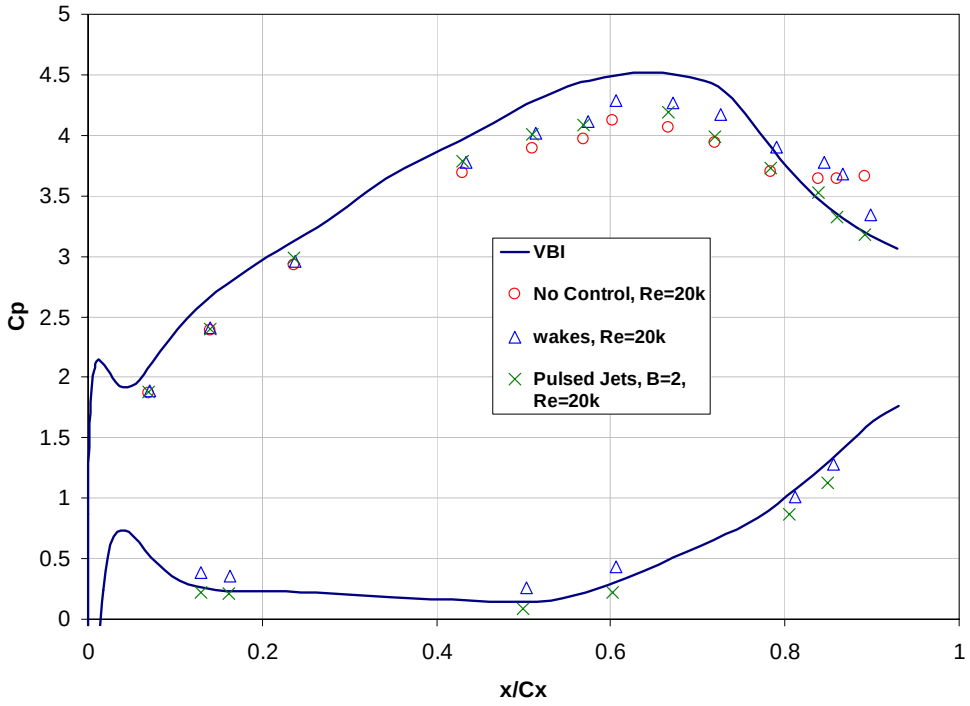

Figure 5-1: c_p distributions along the Pack-B at Re = 20,000 without control, with wakes, and with VGJs as compared to VBI prediction at high Re (non-separating)

PIV data were collected for both the wake and VGJ disturbance conditions. Forty image pairs of velocity were averaged at multiple locations along the pitch spanning 2

VGJ holes. The PIV images were phase-locked at different times throughout the disturbance period. Iso-velocity surfaces were then created from the velocity data at each phase. Figure 5-2 contains the iso-velocity surface (U/U_{in}=0.75) for the no-control data (no induced disturbances). It is provided as a reference for the PIV wake and jet disturbance figures. The flow moves from right to left as depicted by the black arrow. The curvature of the turbine blade has been removed from the surface to isolate the separation region (elevated surface).

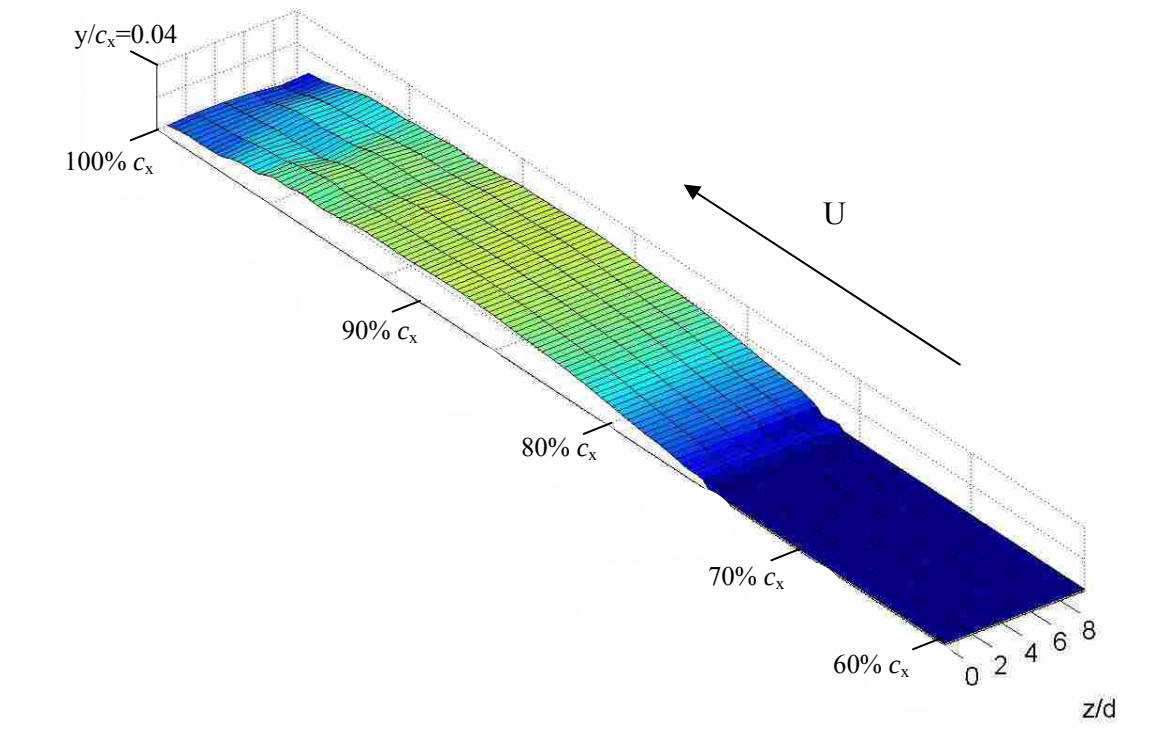

Figure 5-2: Iso-velocity surface (U/U_{in}=0.75) for no-control (no wakes or VGJs). (x/d of 0, 20, 40, and 70 corresponds with c_x of 59, 75, 85, and 100% respectively)

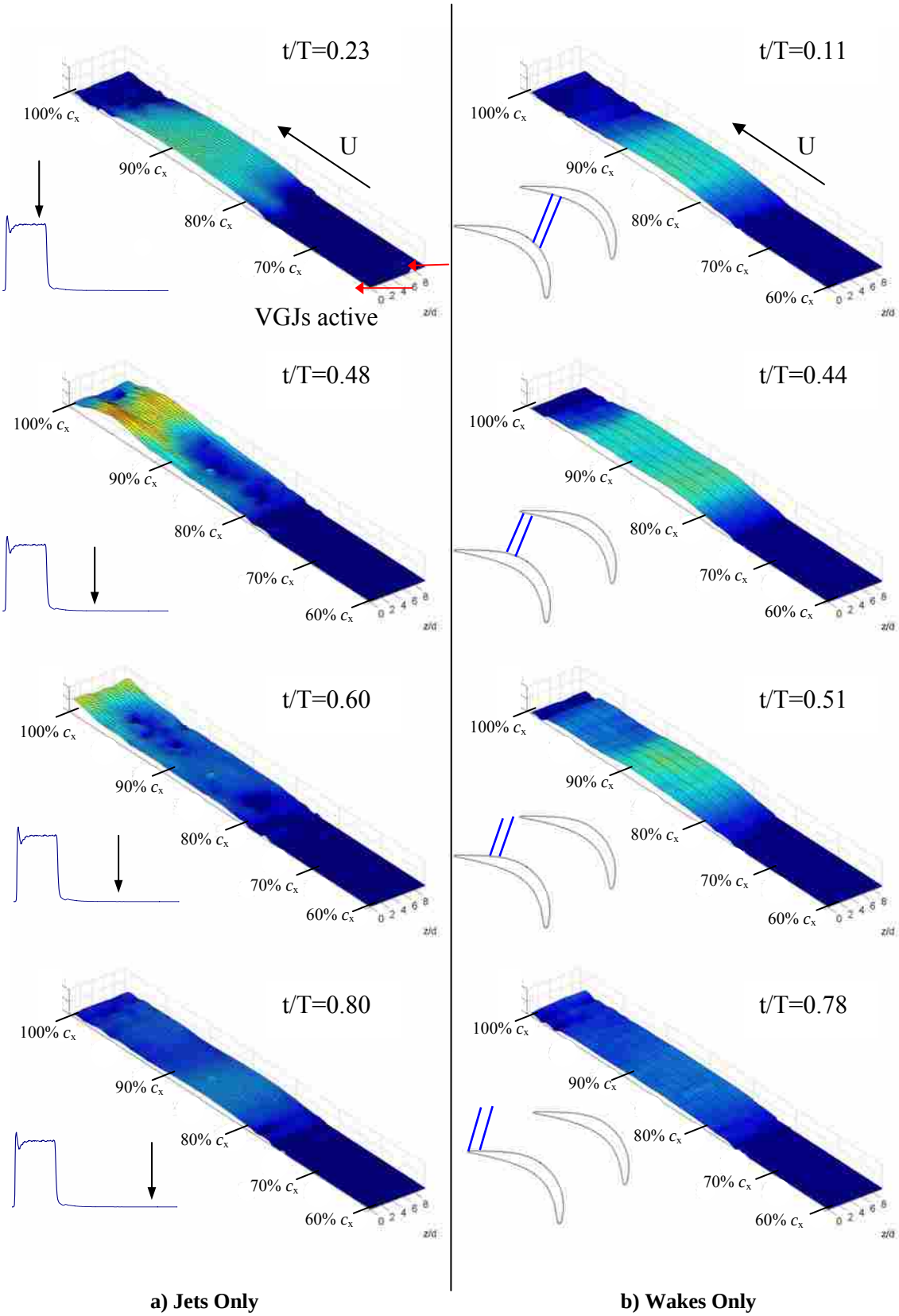

a) Jets Only **b) Wakes Only**

Figure 5-3: Phase-locked iso-velocity surfaces (U/U_{in}=0.75) for jet and wake conditions

Figure 5-3 contains similar iso-velocity surfaces of U/U_{in}=0.75 for the wake and jet data. The iso-velocity surfaces are from the dimensionless times t/T_{wake} of 0.11, 0.44, 0.51, and 0.78 for the wake data, and t/T_{jet} of 0.23, 0.48, 0.60, and 0.85 for the VGJ data. Each figure also includes either a depiction of the jet velocity profile (the black arrow indicates t/T_{jet} position) or the approximate wake location in the passage (represented by blue lines). For the wake data set, the iso-velocity surface of t/T_{wake}=0.11 shows the separation region prior to the impact of the wake disturbance. Subsequent surfaces of t/T_{wake} show the effect of the wake disturbance on the separation bubble. The wake disturbance has a very two-dimensional effect as there is little spanwise variation. By contrast, the jet disturbance initially has a three-dimensional effect as it penetrates the upstream end of the separation region (as shown by the iso-velocity surfaces of t/T_{jet}=0.23 and 0.48 in Figure 5-3(a)). The iso-velocity surface of t/T_{jet}=0.48 depicts the evolution of the initial three-dimensional effect to a two-dimensional effect that is then ejected from the blade. This is further shown in the surfaces of t/T_{jet}=0.60 and 0.80.

As a means of studying the differences between the wake influence and the VGJ influence on the separation bubble in more detail, phase locked velocity data were taken with a hot-film anemometer at a single mid-span location about 2 jet hole diameters above one of the VGJ holes corresponding to z/d=6 in Figure 5-2 and Figure 5-3. Phase-locked plots of mean velocity normalized by the inlet velocity are shown in Figure 5-4. Of the twenty-four phases, every odd phase is displayed in Figure 5-4 through Figure 5-6 for both the wake and the VGJ data sets. In the upper right hand corner of each contour plot is the non-dimensional time value t/T_{wake} for the wake plots and t/T_{jet} for the VGJ plots.

The extent and location of the wake can be seen in both the u_{mean}/U_{in} plots of Figure 5-4(a) and the u_{rms}/U_{in} plots of Figure 5.5 (indicated by the white arrow). The wake enters the data domain near t/T_{wake}=0.15 and its influence can be seen until about t/T_{wake}=0.69. As the wake impacts the separated region it significantly reduces the size of the separation bubble by essentially flattening it, but never completely eliminating the separation. After the wake passes, the residual separation bubble again increases in size before it is impacted by the next wake. The influence of the VGJ on the separation bubble can be seen in Figure 5-4(b). The jet pulse initiates immediately after t/T_{jet}=0.02 and ends just after t/T_{jet}=0.27 (note white arrows). The pulse influence can be seen upstream of the separation bubble from t/T_{jet}=0.10 through 0.35. This near wall jet disturbance causes the separation region to bunch up as it pushes the entire bubble off the back of the blade. As the bunched separation region is being wiped off the blade a new separation bubble begins to form and re-grow. The bunching and pushing back of the separation bubble can also be seen in the iso-velocity surface plot of Figure 5-3. Since the hot-film data were taken along a spanwise location of significant jet influence (near z/d=6), the bubble dynamics as seen in Figure 5-4(b) and Figure 5-5(b) will not be exactly the same at other z/d locations. More will be discussed on this later. The initial penetration of the VGJ into the separation bubble is very distinct at the location of this hot-film data.

Evidence of the control mechanisms for both the wake and the VGJ data can be seen in the contour plots of u_{rms}/U_{in} in Figure 5-5. Again, every odd phase is displayed showing 12 of the 24 phases for both cases. The natural breakdown of the separated free shear layer can be seen by the elevated u_{rms} levels off the wall at y/c_x~0.02 in both the

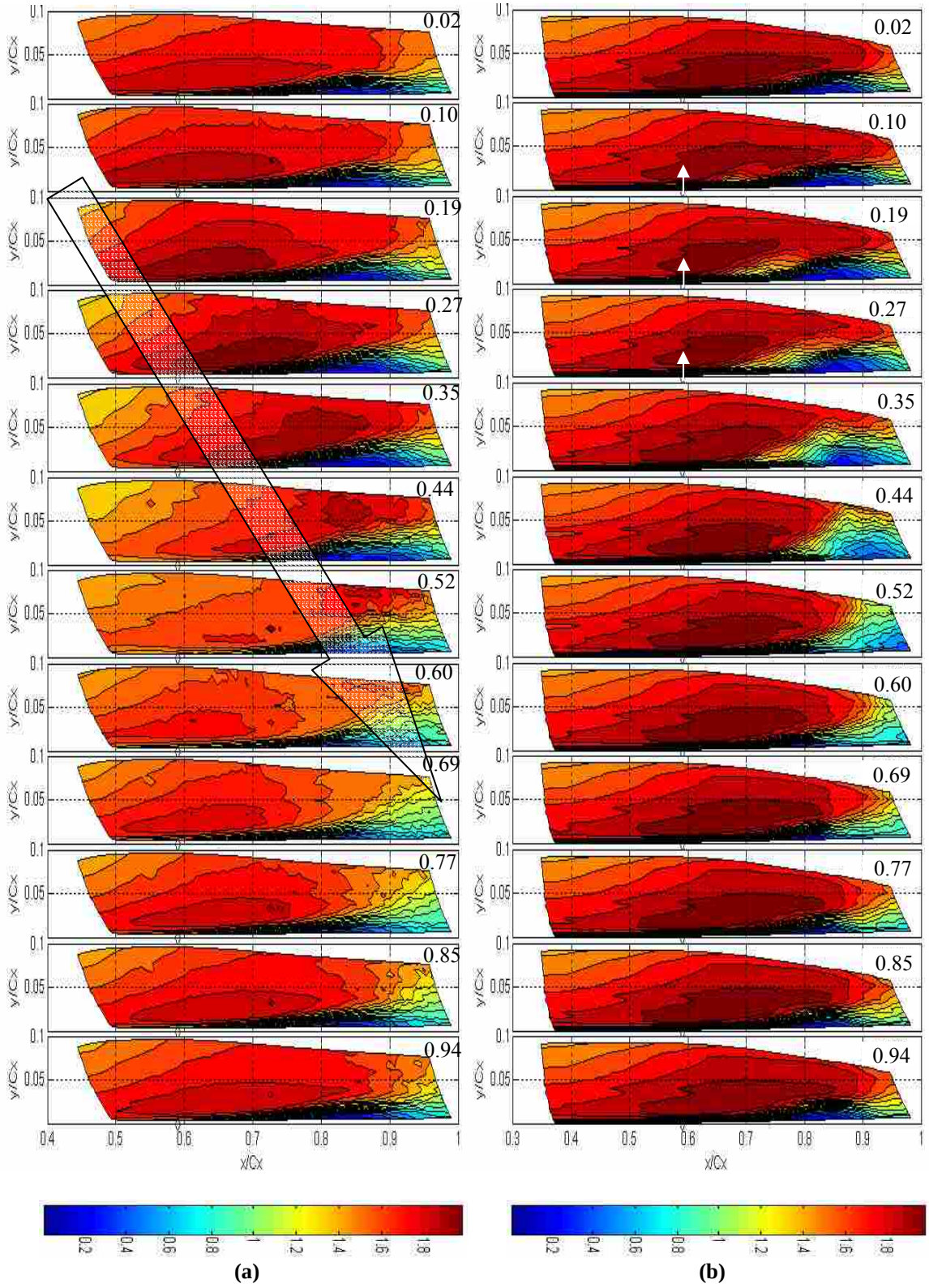

Figure 5-4: Phase-locked contour plots of u_{mean}/U_{in} for (a) wake and (b) VGJ conditions with white arrows indicating VGJ on times

wake and the jet data at around 86% c_x, before the wake or jet influence has arrived (t/T=0.02-0.10). The turbulent disturbance of the wake causes unsteadiness and rapid bypass transition of the separated shear layer all the way up near 70% c_x by t/T_{wake}=0.35. Not only does the wake induce early breakdown of the shear layer but also it causes elevated levels of turbulence over the separated region. Even though the turbulent breakdown of the shear layer reduces the separation size it does not fully eliminate it. The separated region below the shear layer can still be seen as a thin zone of low turbulence underneath the shear layer even as the wake is passing over it at t/T_{wake} of 0.35 and 0.44. As the wake continues off the blade, it leaves behind levels of relatively low turbulence. Gostelow and Thomas [14, 15] refer to this region of low turbulence as a "calmed zone" and also show evidence of this wake-induced bypass transition [14]. While the wake influence on the separation bubble starts in the free shear layer, the jet introduces high levels of near-wall turbulence upstream of the separation bubble (t/T_{jet}=0.10). As the highly turbulent influence of the jet convects downstream it stays close to the wall and penetrates the separation bubble, causing it to bunch up and convect off the blade. A new separation bubble begins to form as soon as the old bubble leaves. For the VGJ case, the residual levels of turbulence in the shear layer never drop as low as the calmed region seen after the passing of the wake.

Contour plots of intermittency also show these different control mechanisms (Figure 5-6). It should be noted that in these plots all values of intermittency less than 0.97 were set to zero to more clearly show the laminar and fully turbulent regions. Turbulent transition naturally occurs as shear layer breakdown which can be seen in the

initial phases of the intermittency plots for both the wake and the jet conditions near 85% c_x ($0.1 \leq t/T \leq 0.27$). The wake disturbance causes the shear layer to breakdown earlier as shown by the upstream movement of the transition line in t/T_{wake}=0.44-0.52. As the wake exits the data domain it nearly re-laminarizes the flow creating the calmed zone (t/T_{wake}=0.94, 0.02, 0.10). The jet acts as a source for near-wall turbulent transition well upstream of the natural transition location (t/T_{jet}=0.10). The region of turbulent flow from the jet convects downstream until merging with the naturally transitioning flow in the shear layer, eventually filling the flow domain along the aft portion of the blade with turbulent flow. Although the jet seems to more successfully reduce the separation bubble, it does not reduce the size of the turbulent region as much as the wake does.

Time-space plots of u_{mean}/U_{in}, u_{rms}/U_{in}, and intermittency were created at an elevation of 6.2mm off the wall for both wake and VGJ conditions (Figures 5-7, 5-8, and 5-9 respectively). As the bubble is suppressed in both cases, regions of previously low velocity along the aft portion of the blade ($0.8<c_x<0.97$) increase in velocity reaching magnitudes of U_{mean}/U_{in} greater than 1.2. The amount of time that the flow is able to maintain this elevated velocity is greater for the jets as compared to the wake disturbance. This region is highlighted in Figures 5-7(a) and (b) by the green ovals. The jet influence maintains this higher velocity for nearly twice as long as the wake disturbance at this y/c_x elevation. Again, this is consistent with previous discussion indicating that the wake produces a gradual thinning of the separation bubble while the jet pushes the bubble off the blade altogether.

Since these time-space plots are at an elevation within the shear layer, it is easy to see how the wake influences the shear layer differently than the jet. In Figure 5-8, much

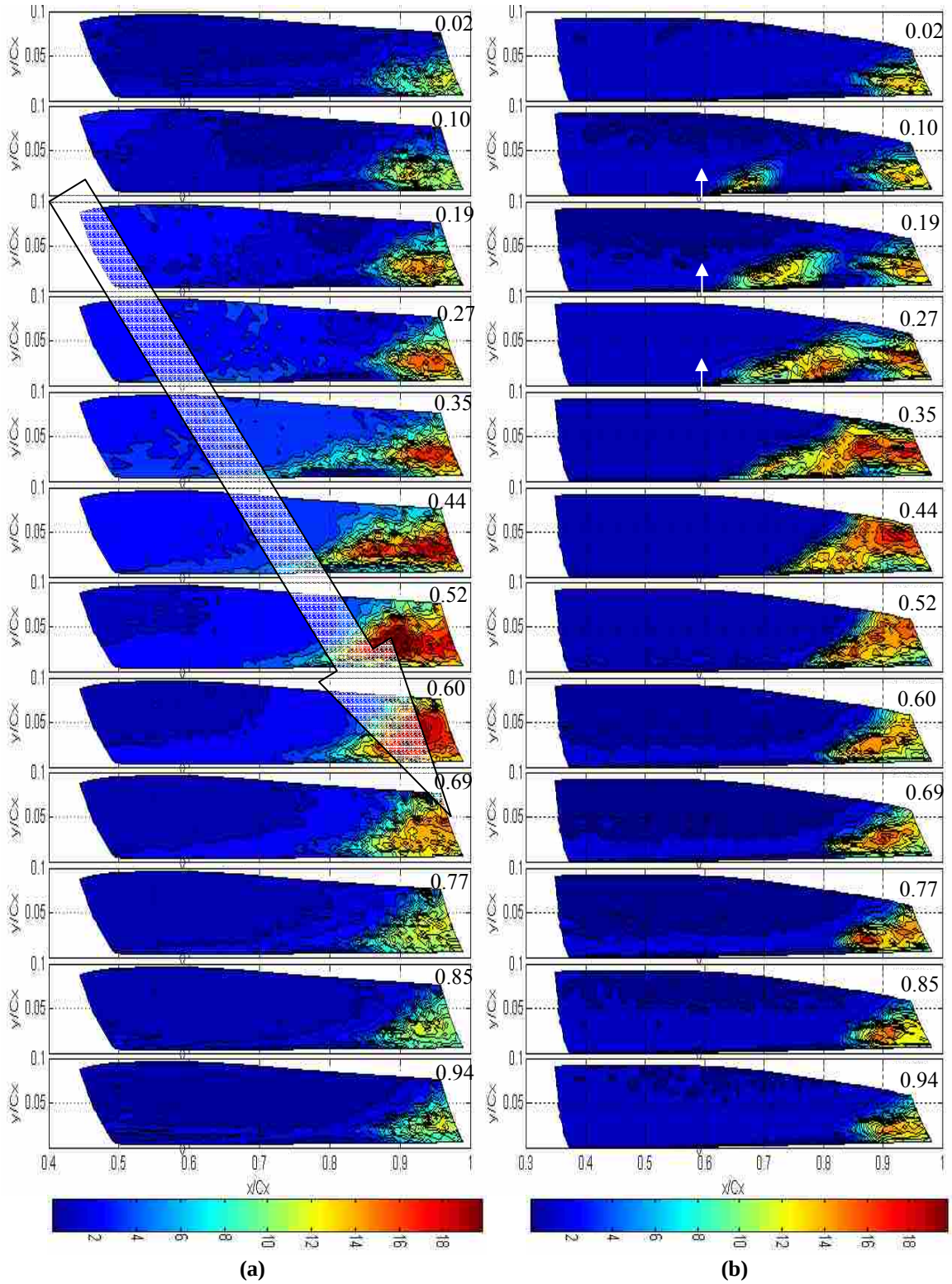

Figure 5-5: Phase-locked contour plots of u_{rms}/U_{in} for (a) wake and (b) VGJ conditions with white arrows indicating VGJ on times

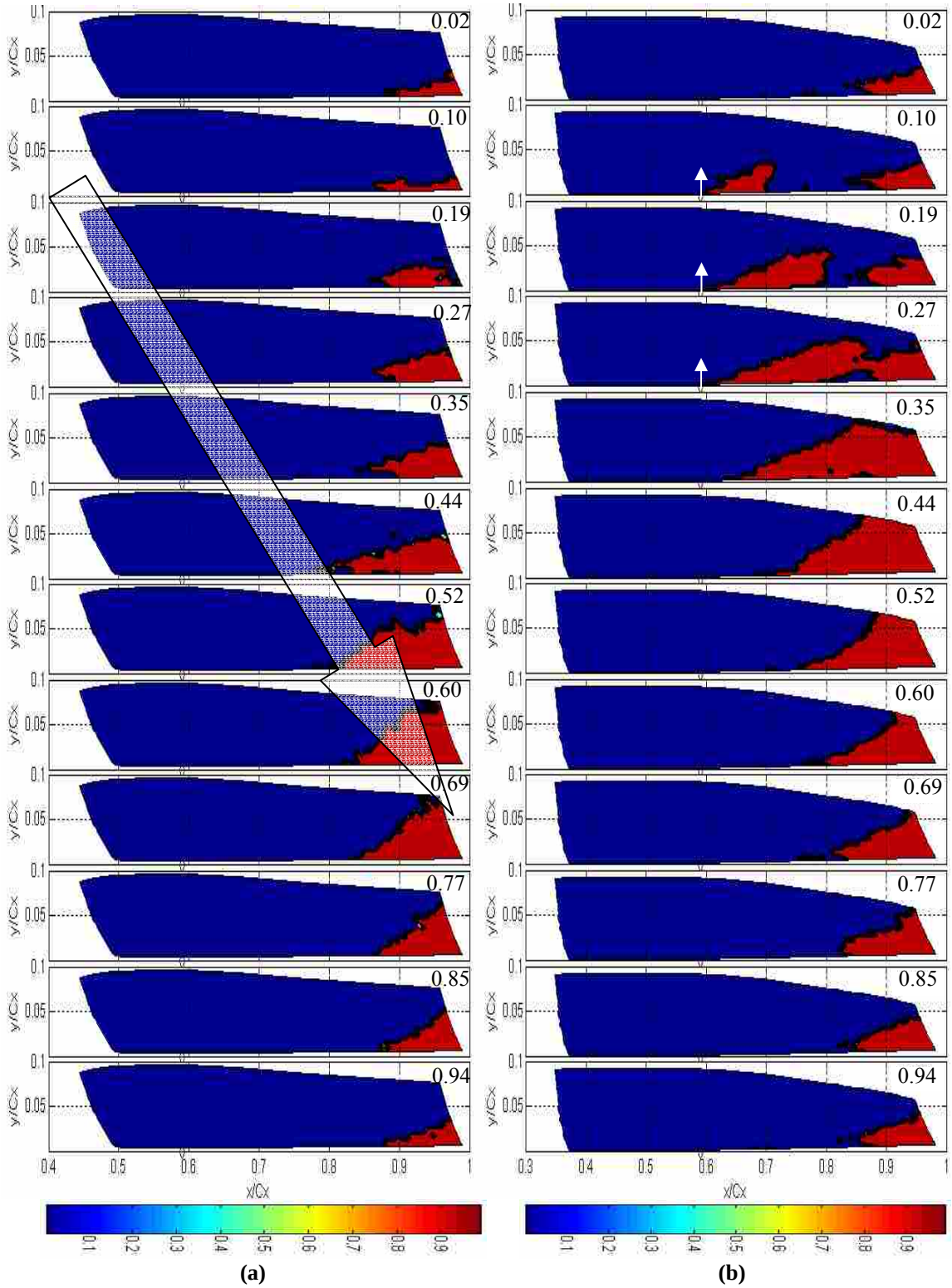

Figure 5-6: Phase-locked contour plots of Intermittency for (a) wake and (b) VGJ conditions with white arrows indicating VGJ on times

higher levels of turbulence occur from the wake influence as it amplifies the unsteadiness of the free-shear layer. The jet influence does not have a comparable amplifying effect on the free-shear layer since it penetrates from the wall. The region of low turbulence after the disturbance passes, or a calmed zone, is greater and lasts much longer due to the passing of the wake than it does due to the passing of the jets influence. This region has been highlighted by black ovals in Figure 5-8.

From the (unfiltered) intermittency time-space plots of Figure 5-9 it can be seen that transition happens rapidly for both the wake and the jet conditions as evidenced from the very narrow transition bands. As the wake starts to impact the separation region near t/T_{wake}=0.4, the location of transition quickly jumps from near 86% to about 81% c_x. However, the location of transition subsequently moves down the blade much more slowly from the wake influence than it does due to the jet influence. These trajectories are highlighted by the transparent white arrows. The migration of the transition location due to the jet disturbance is close to 2 times that of the wake disturbance at this elevation. This is because the jet forces early near wall transition resulting in fully turbulent flow to convect downstream near freestream velocities. However, the wake causes the shear layer to become unsteady. This unsteadiness propagates toward the wall and downstream slower than freestream velocities. The transition location due to the jet ultimately stops at around 85% c_x and remains there until the jet is pulsed again. The transition location due to the wake migrates down to nearly 95% c_x in the calmed zone before quickly moving back to a "steady state" upstream location around 85% c_x before the impact of the next wake. The data in these figures suggest that VGJs could perhaps be

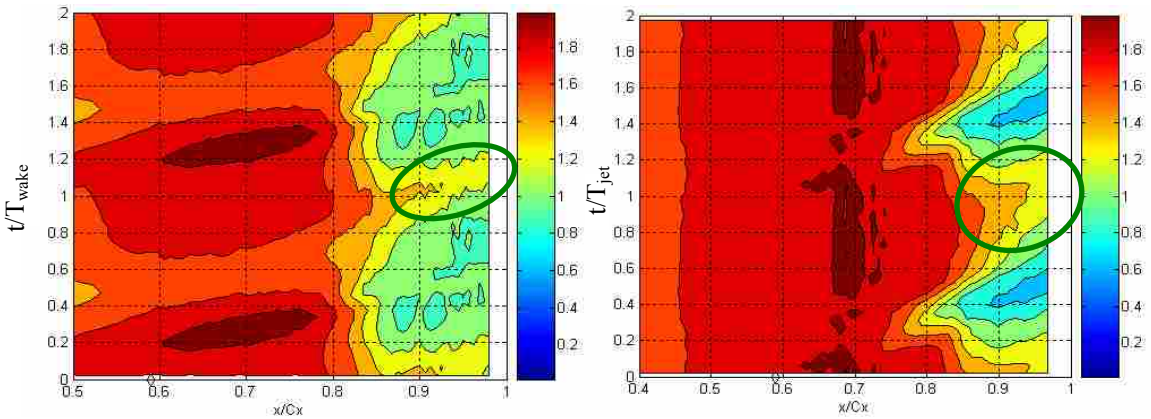

Figure 5-7: Time-space contour plots of Umean/Uin for (a) wake and (b) VGJ conditions 6.2 mm from blade surface

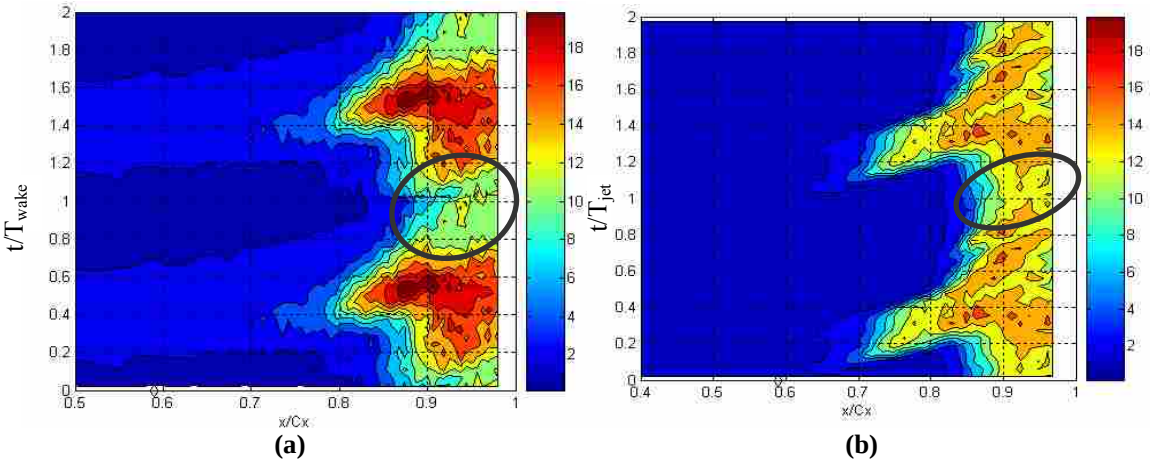

Figure 5-8: Time-space contour plots of Urms/Uin for (a) wake and (b) VGJ conditions 6.2 mm from blade surface

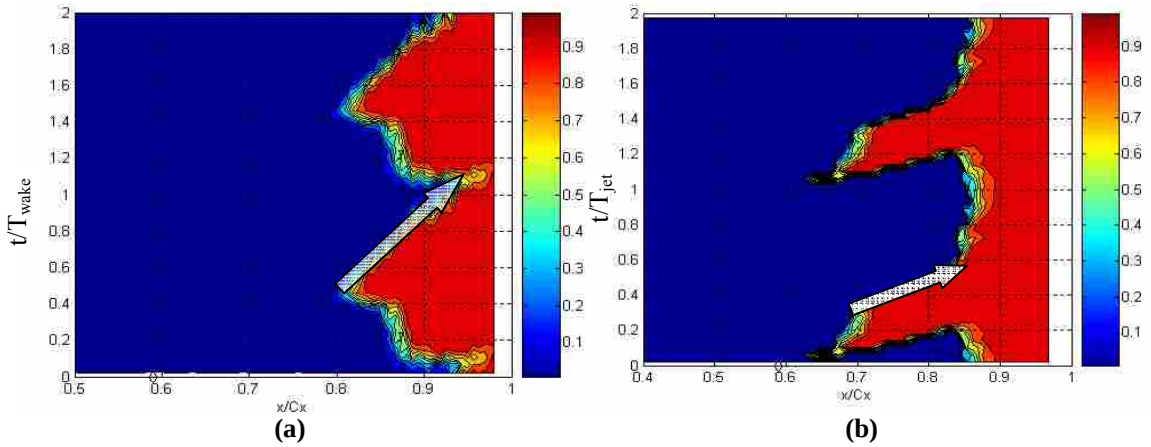

Figure 5-9: Time-space contour plots of intermittency for (a) wake and (b) VGJ conditions 6.2 mm from blade surface

synchronized together with the wakes to achieve even greater separation reduction with an extended calmed zone.

5.2 Spanwise influence of VGJs

Although the VGJ influence results in a reduction of the separation region along the entire blade span, initially the discrete VGJ event is very three-dimensional as seen in Figure 5-10. Figure 5-10 contains four iso-velocity surface plots of U/U_{in}=1.3 at four phases in the VGJ period. Figure 5-10(a) is at time t/T_{jet}=0.23, right before the jet turns off, and Figure 5-10(b) is at time t/T_{jet}=0.35, right after the VGJ turns off. Figures 5-10(c) and (d) are later in the pulsing cycle as the jet effect has become nominally spanwise uniform and the separation region is reduced. In both Figures 5-11(a) and (b) the initial VGJ impact on the separation region is clearly not spanwise uniform. In order to better understand the transitional influence of the VGJs at different spanwise locations, a second set of follower data were taken at a spanwise elevation of z/d=2.7. The first set of follower data were taken at z/d=6. The locations of follower data acquisition with respect to the jet disturbance are marked on Figure 5-10 (as red lines and yellow dashed lines) as well as on Figure 5-11 (as white dashed lines). At these two locations the most dynamic spanwise differences of VGJ influence on the separation bubble can be captured, as highlighted by the green and white arrows on Figure 5-10(b). Figure 5-11 contains contour plots of u_{mean}/U_{in} which were extracted from the PIV data at 5 phases of VGJ period. These plots show velocity contours in the x-z plane 2mm from the blade surface. The vertical axis on the plot is the spanwise location relative to the bottom of a

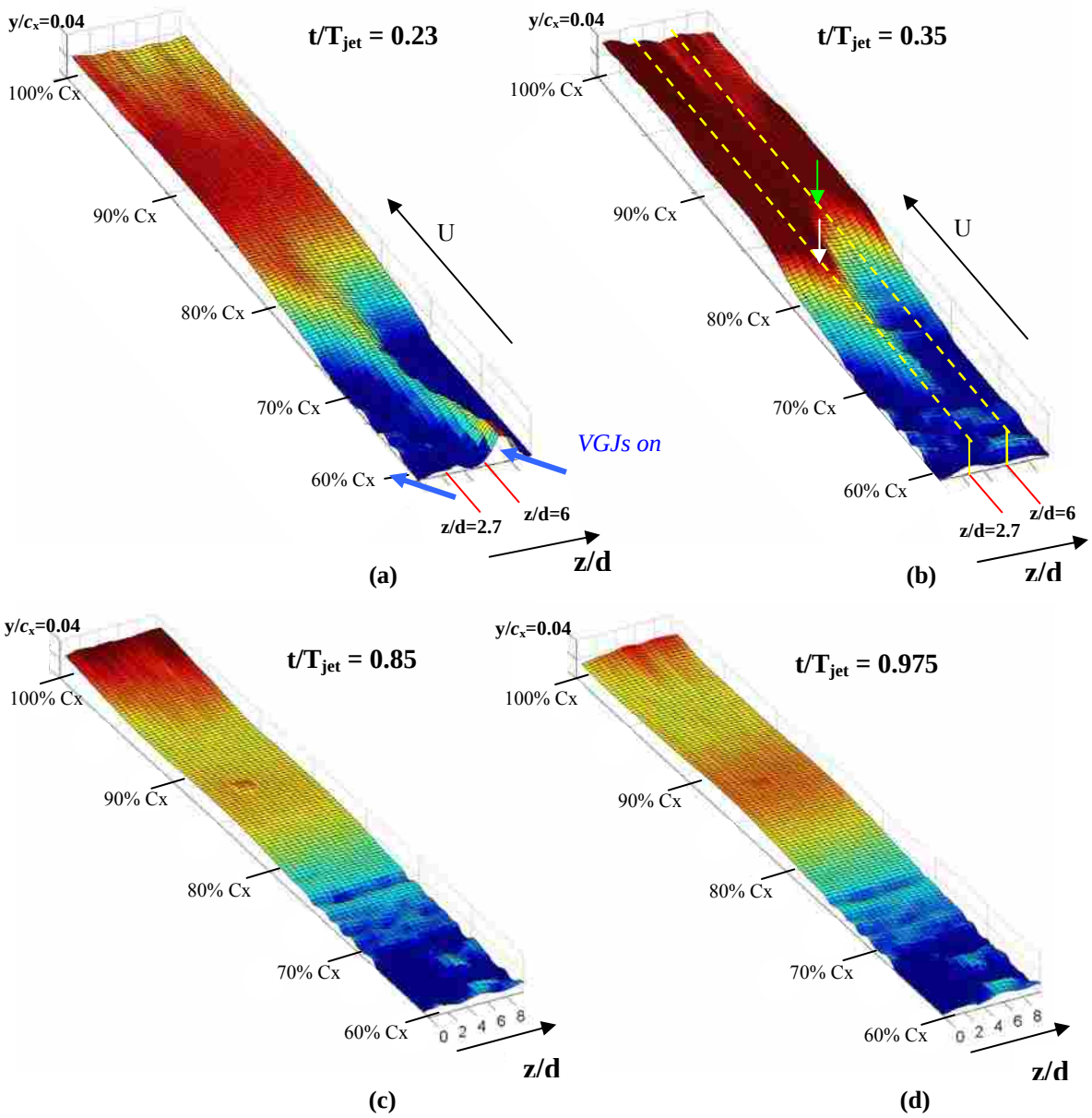

Figure 5-10: Iso-velocity surface plots of U/U_{in}=1.3 at (a) t/T_{jet}=0.23, (b) t/T_{jet}=0.35, (c) t/T_{jet}=0.85, and (d) t/T_{jet}=0.975

VGJ hole in jet hole diameters, and the horizontal axis is the axial chord location (% c_x). The VGJ location is identified by the black ovals while the region of jet influence is circled by the blue ovals. Eldredge [8] showed that during steady VGJ operation, streamwise vortices migrate up along the blade span (negative z-direction) as well as

away from the blade wall for the same VGJ orientation. Figure 5-11 shows that the region of jet influence from the pulsed jet also migrates along the span as it is convected downstream. At t/T_{jet}=0.10 the jet influence has already crossed the z/d=6 follower plane. By t/T_{jet}=0.23, the jet has been on for nearly its full duration and its influence is present from z/d=8 to about z/d=2. After the jet is turned off, the remaining VGJ fluid

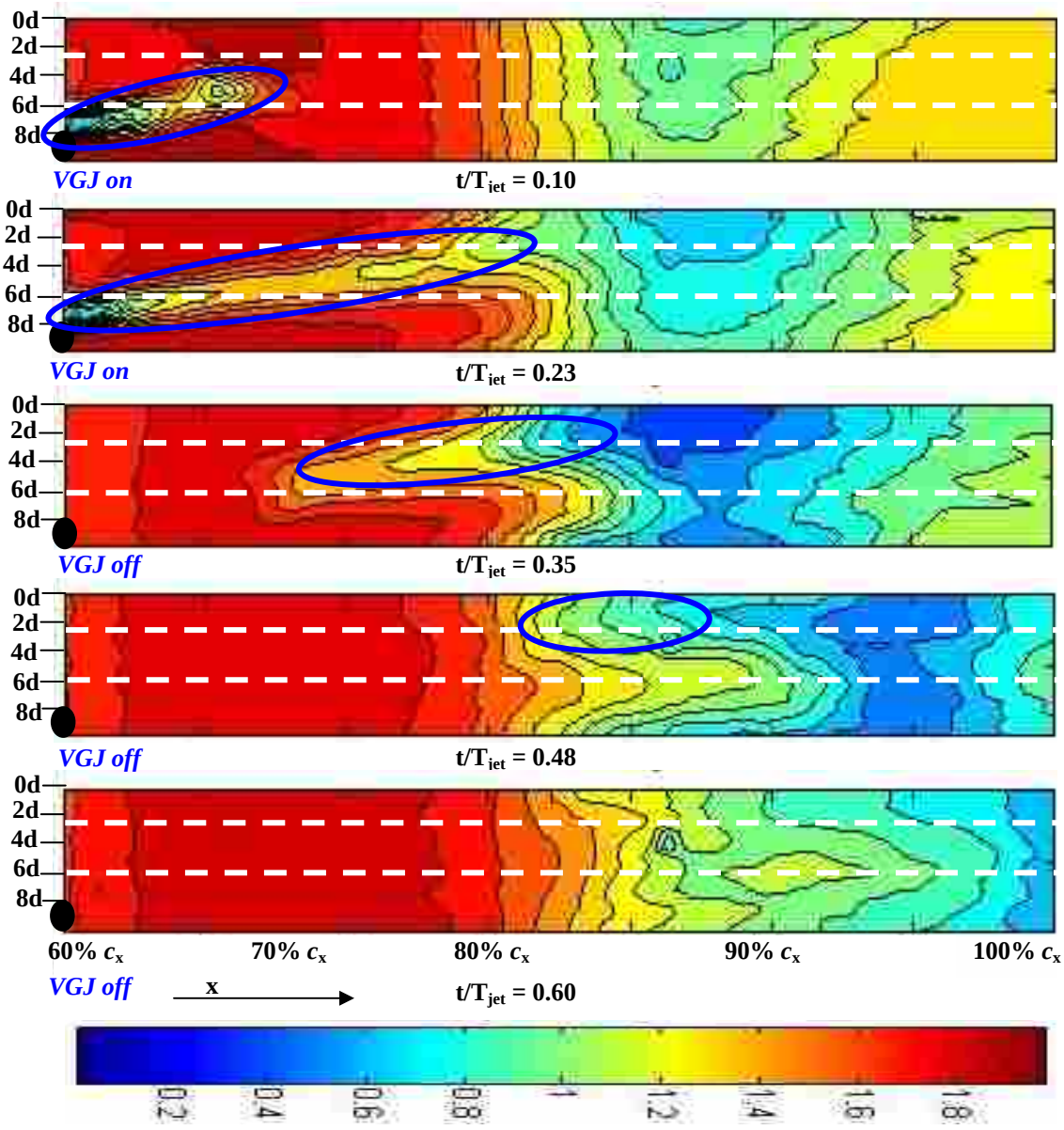

Figure 5-11: Contour plots of u_{mean}/U_{in} in x-z plane, 2mm from wall

migrates up along the span and convects downstream. At t/T_{jet}=0.35 the jet is no longer present at the z/d=6 elevation, but continues to be influential at the z/d=2.7 elevation through t/T_{jet}=0.48. By t/T_{jet}=0.48 it appears that the jet fluid has lost much of its spanwise momentum and is being more fully entrained by the freestream flow. By t/T_{jet}=0.6 the strong jet influence has mostly disappeared while its effects begin to dissipate out along the span as the separation bubble gets pushed off the blade in a spanwise uniform manner. At times t/T_{jet}=0.10 through 0.35 it can be seen that the region of strongest jet influence crosses the z/d=6 follower plane at about 65% c_x while it crosses the z/d=2.7 follower plane further downstream at about 75% c_x. From these plots it also appears that the jet crosses about 60% of the hole pitch before dissipating.

The follower data at the locations z/d=6 and 2.7 are presented in Figures 5-12 through 5-14, and contain u_{mean}/U_{in}, u_{rms}/U_{in}, and intermittency. Again, these plots show every odd phase of the 24 phases from the phase-locked follower data. Contour plots of u_{mean}/U_{in} in Figure 5-12 show that the jet influence has a very similar effect on the separation bubble at an elevation of z/d=2.7 (Figure 5-12(a)) as it does at z/d=6 (Figure 5-12(b)). After the jet actuates, it causes a bunching up of the separation region as the separation region is pushed off the back of the blade. However, as expected, the jet influence on the separation bubble at a span elevation of z/d=2.7 is seen about one phase after the effects of the jet at z/d=6. It also appears that the separation bubble at z/d=2.7 sees a greater separation reduction which is evidenced by the smaller region of low velocity fluid at the final and initial phases and is highlighted by yellow ovals.

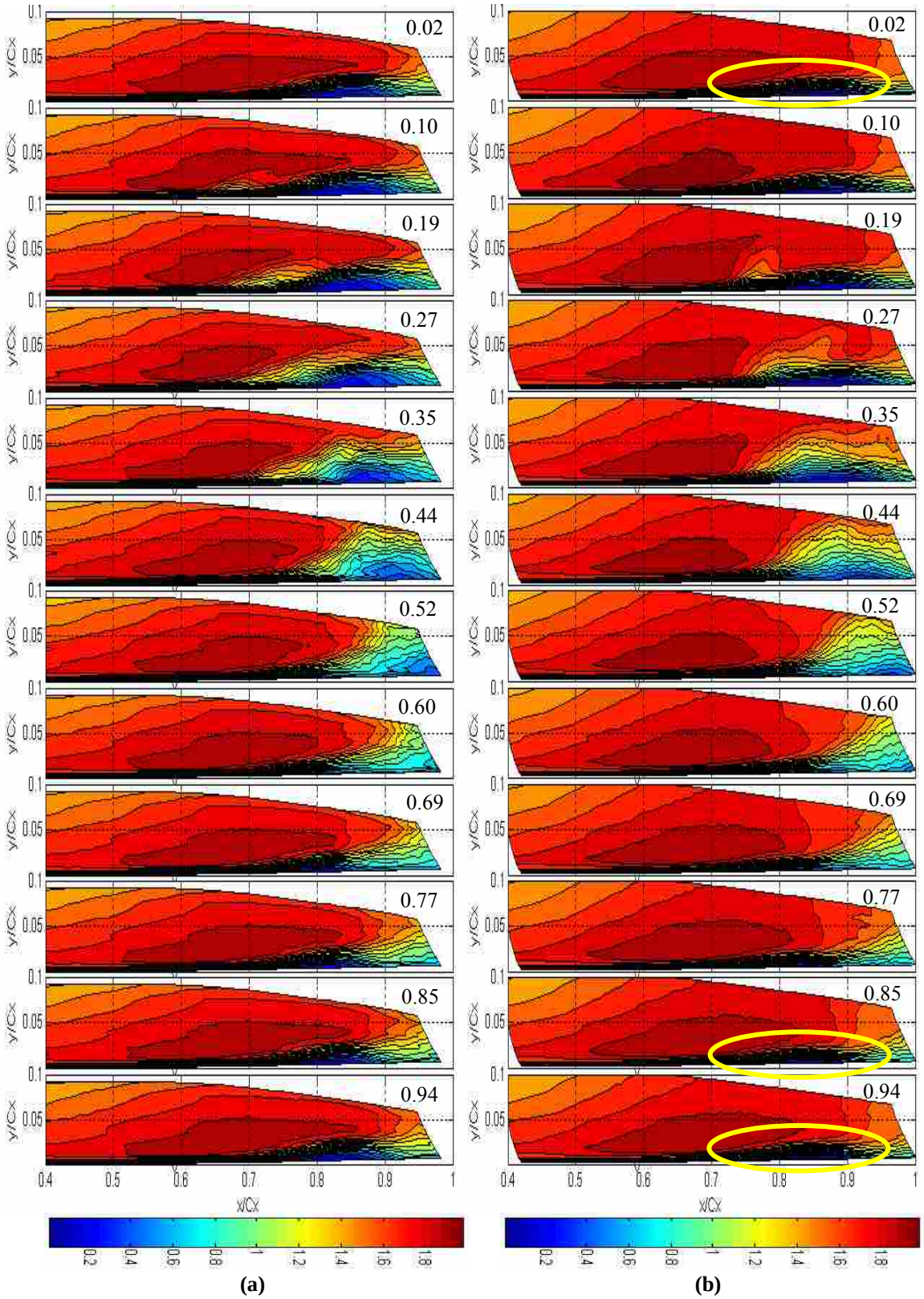

Figure 5-12: Contour plots of u_{mean}/U_{in} at spanwise locations (a) z/d=6 and (b) z/d=2.7

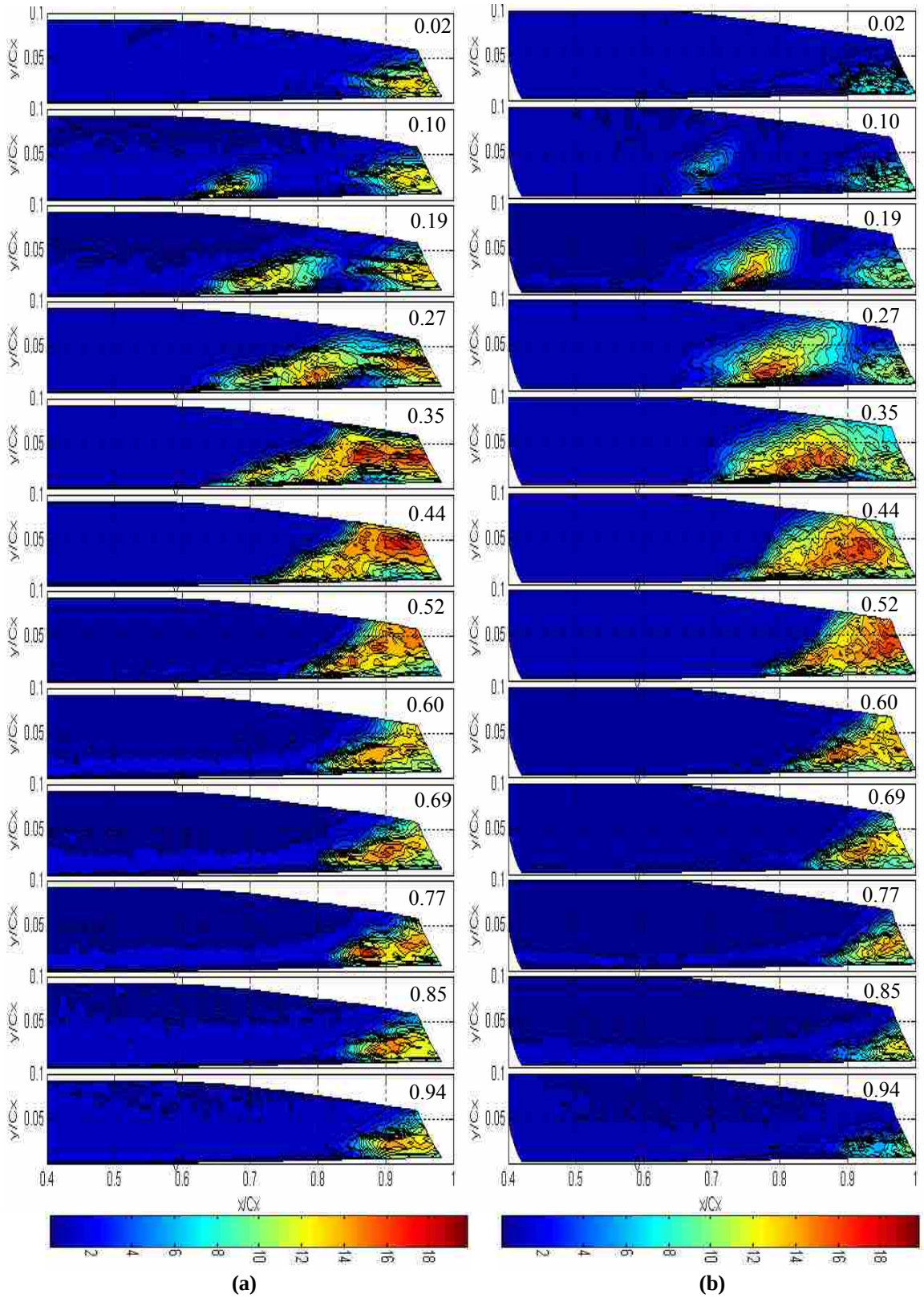

Figure 5-13: Contour plots of u_{rms}/U_{in} at spanwise locations (a) z/d=6 and (b) z/d=2.7

Figure 5-13 contains contour plots of u_{rms}/U_{in} at span elevations of z/d=6 and 2.7. Like the u_{mean}/U_{in} plots of Figure 5-12, the jet influence at z/d=2.7 is seen shortly after it appears at z/d=6. However, the jet influence at z/d=2.7 is seen not only later, but it is initially seen further downstream as well as further from the blade surface. At the z/d=6 elevation the jet is seen as a highly turbulent near wall disturbance which impacts the separation region and essentially overtakes the separation region with high turbulent flow. At the z/d=2.7 elevation the turbulent jet disturbance impacts the separation zone further from the blade surface, causing the turbulence to spread towards the wall as well as downstream seen in phases t/T_{jet}=0.19-0.35. It can also be seen in the final phases of Figure 5-13 that the calmed region along the aft portion of the blade shows turbulence intensities at z/d=2.7 of about half of what they are at z/d=6. This can be attributed to the jet influence more directly impacting the separation region further aft on the blade rather than convecting down the blade as an upstream disturbance. Likewise, these results are further substantiated by the filtered intermittency plots in Figure 5-14. At a spanwise elevation of z/d=6 the jet is seen as a near wall disturbance which causes turbulent transition. The transitioned flow near the wall impacts the separation region and overwhelms the aft portion of the blade with turbulent flow. At the z/d=2.7 elevation the jet also acts as a source for turbulent transition, but again it appears further away from the blade surface and nearly 10% c_x further downstream, causing early breakdown of the separated shear-layer similar to the wake disturbance. Phases t/T_{jet}=0.94 and 0.02 from Figure 5-14(b) show a calmed region where the jet nearly re-laminarizes the entire flow domain along the back of the blade.

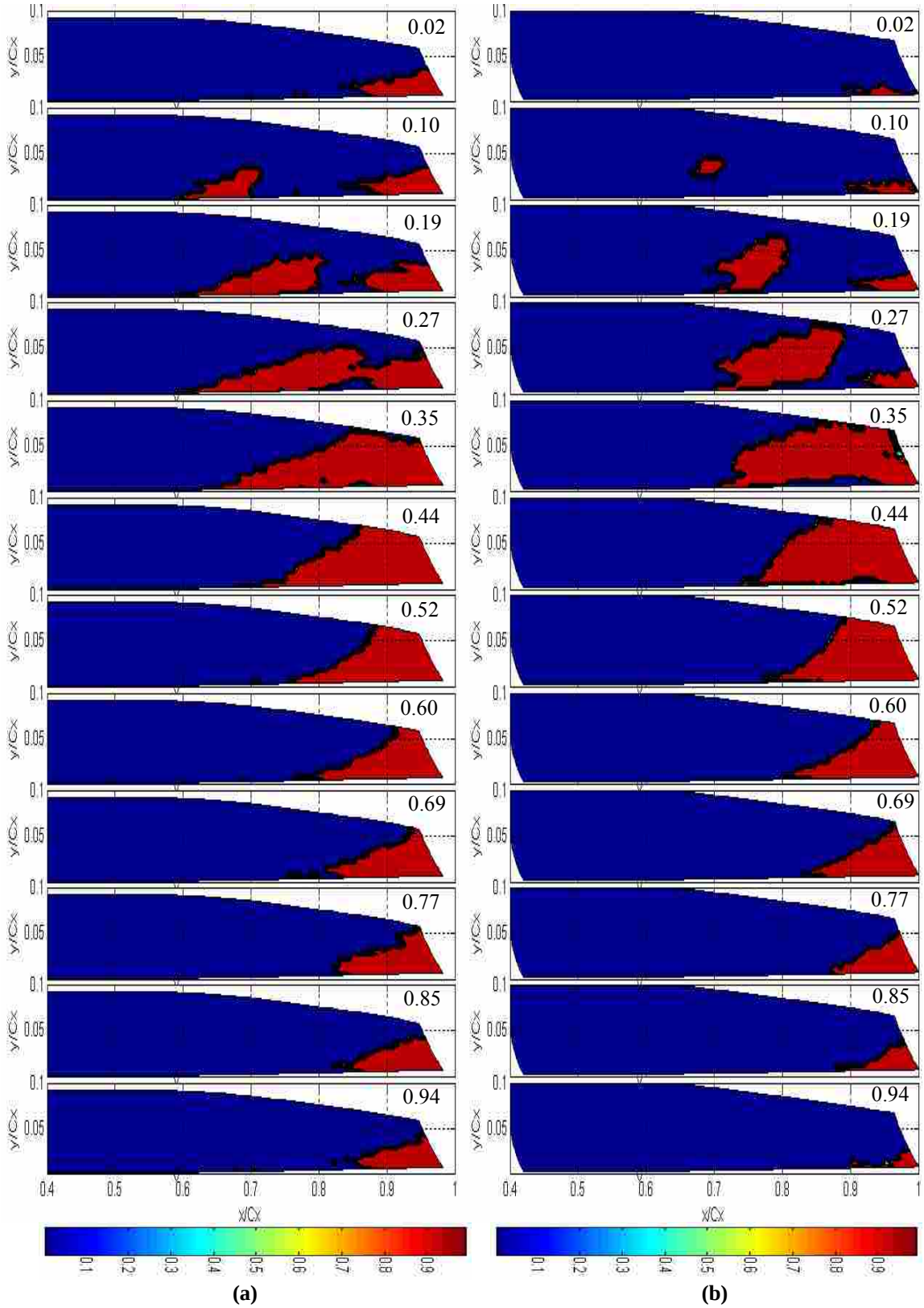

Figure 5-14: Contour plots of intermittency at (a) z/d=6 and (b) z/d=2.7

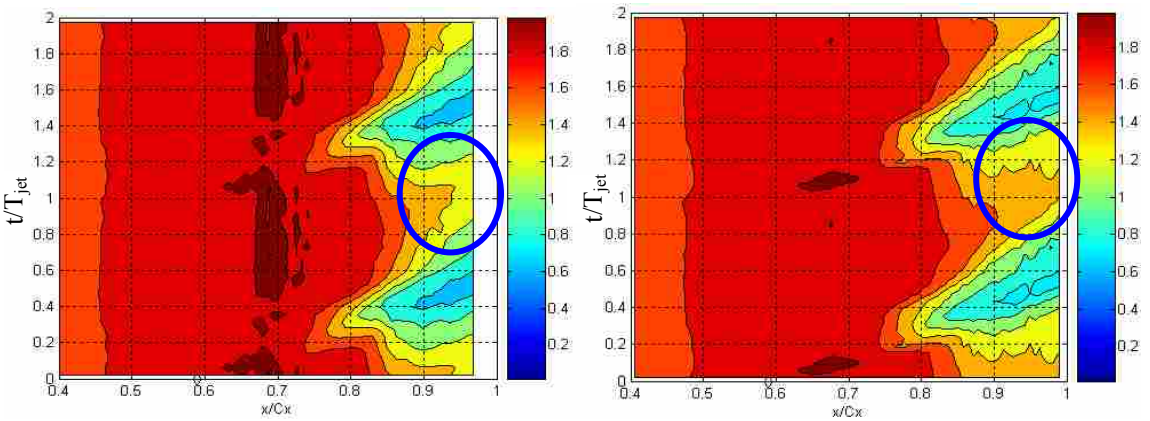

(a) z/d=6 **(b) z/d=2.7**

Figure 5-15: Time space plots of u_{mean}/U_{in} at (a) 6.2mm and (b) 6.1mm from blade surface

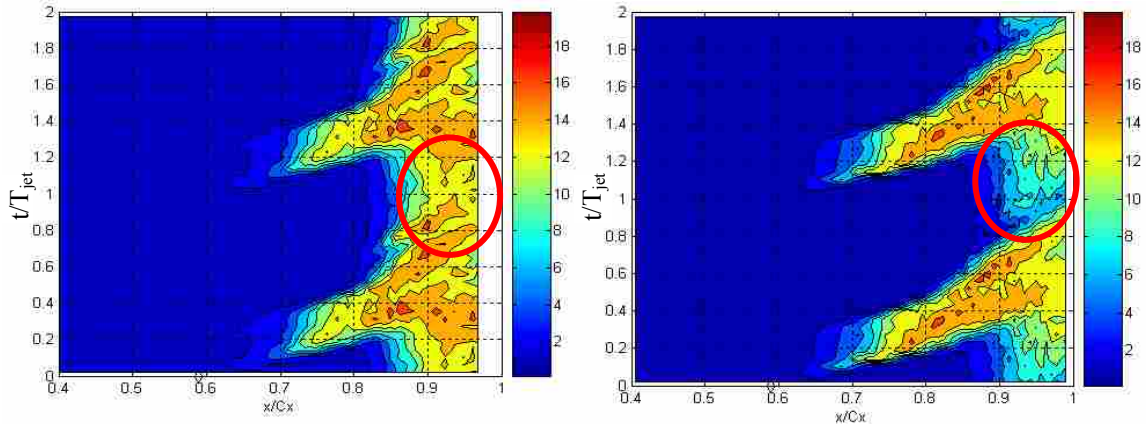

(a) z/d=6 **(b) z/d=2.7**

Figure 5-16: Time space plots of u_{rms}/U_{in} at (a) 6.2mm and (b) 6.1mm from blade surface

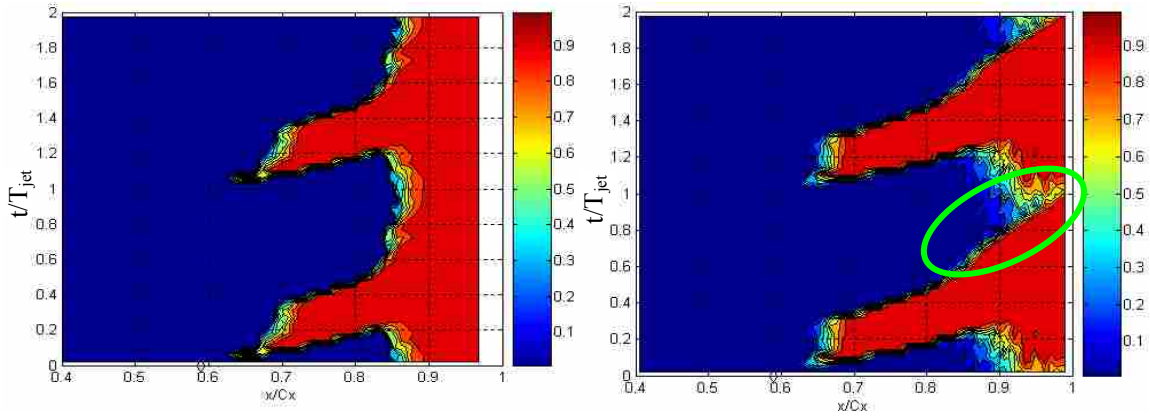

(a) z/d=6 **(b) z/d=2.7**

Figure 5-17: Time space plots of intermittency at (a) 6.2mm and (b) 6.1mm from blade surface

Time-space plots of u_{mean}/U_{in}, u_{rms}/U_{in}, and intermittency (unfiltered) are presented in Figures 5-15, 5-16, and 5-17 respectively. They are at a wall distance of 6.2mm for the z/d=6 spanwise location (as shown previously) and at a wall distance of 6.1mm for the z/d=2.7 spanwise location. The blue ovals of Figure 5-15(a) and (b) show that at a spanwise elevation of z/d=2.7 the jets are more effective at reintroducing high velocity flow near the wall along the aft portion of the blade. This is likely due to the more direct impact of the jet onto the separation region at this elevation resulting in greater separation reduction. Not only does the velocity increase along this portion of the blade at z/d=2.7 but the turbulence levels are about half of what they are at z/d=6 (Figure 5-16). This is also seen in the intermittency plot of Figure 5-17. From t/T_{jet}=0 to 0.5 the location of transition moves downstream as a result of the jet influence in both Figure 5-17(a) and (b). However, from t/Tjet=0.5 to 1, the location of transition reaches a "steady state" value of around 85% c_x at the z/d=6 location but at the z/d=2.7 location the location of turbulent transition continues to migrate downstream to nearly 100% c_x (as highlighted by the green oval). From t/T_{jet}=1 to 1.2 the location of transition slowly moves back upstream until about 90% c_x before being impacted by the next VGJ pulse.

This additional plane of follower data shows distinct differences in transition behavior along the span between VGJ holes. These differences can be explained by the location and migration of jet influence resulting from a single pulse of the VGJs. Due to the shallow angle of the jet with respect to the blade surface, a broad spanwise region is affected by the VGJ. Provided the jet hole spacing is small enough so that the jet effect on the separation merges into a 2-D wave before the trailing edge, the net effect is similar to the effect of a wake. However, even though the net effect of separation reduction may

be similar for jets and wakes, the control mechanisms of jets are different than that of wakes and vary along the hole pitch. Also, because the locations of follower data acquisition were located at spanwise locations of greatest dynamic differences (indicated earlier by white and green arrows in Figure 5-10(b)), other spanwise locations will likely exhibit similar behaviors seen in the z/d=6 and 2.7 follower planes.

6 Conclusions

Hot-film measurements were taken in a low speed low pressure turbine cascade to obtain detailed, unsteady velocity and turbulence data in two separating boundary layers. Data were taken for two different blade profiles, a mid-loaded L1M and an aft-loaded Pack B design, under both pulsed VGJ controlled and no control conditions. Comparisons were made between the separation characteristics as well as the control characteristics and separation regrowth for each set of blades. Flow separation characteristics differed for the L1M which had a separating, reattaching boundary layer, and the Pack B which had a separating, non-reattaching boundary layer. Without flow control, the separating laminar shear layer on the Pack B remained stable for nearly twice as long as the L1M before experiencing turbulent breakdown. Due to the delayed shear layer transition, the Pack B separation did not fully reattach to the blade, unlike the L1M. Separation control for the L1M showed significantly less benefit (in terms of bubble size reduction) due to the upstream location of the bubble. Once the bubble was swept off, separation regrowth began immediately until the jet pulsing cycle restarted. For the Pack B blade, bubble regrowth was not evident for nearly 35% of the pulsing cycle after the separation bubble had been convected off the blade. This may be due to the increased flow inertia caused by the large amplitude flow oscillations inherent with the control of large, non-reattaching separations.

Unsteady velocity measurements were also made in the presence of periodic unsteady wakes and pulsing vortex generating jets on the Pack B profile. Comparisons were made between the separation characteristics as well as the control characteristics for both cases. In the presence of unsteady wakes, the separation bubble is reduced in size and flattens as the wake passes over. This is caused by the unsteadiness found in the wake which triggers early transition of the separated shear layer. The effect of the wake disturbance propagates down towards the wall, reducing the separation size as long as the wake is passing over. As the wake leaves, a calmed region of low turbulence flow is left behind.

The VGJ influence causes a 3-D near wall disturbance which convects downstream and impacts the separation bubble. The bubble then bunches up and convects off the trailing edge of the blade. As the bunched separation bubble is pushed off the blade, a new separation bubble begins to form and continues to grow until the impact of the next jet. In essence, the VGJ acts as source for turbulent transition which convects downstream, impacting the separation zone. As the VGJ disturbance convects downstream it also migrates up along the span of the blade providing control for the entire VGJ hole pitch. Detailed 3-component PIV measurements by Bloxham et al. [28] show evidence of vortices as well, but these are thought to have a secondary effect on separation dynamics. The results from this study show promise for the synchronization of VGJs and wakes to achieve synergistic benefits.

The results from these studies contribute further clarification about the role transition plays in separation dynamics in the presence of pulsing VGJs and unsteady wakes. It is also beneficial to future low pressure turbine blade designers in helping

create designs which are ideally suited for VGJ implementation. Designing new turbine blades with integrated active flow control can help continue the current trend towards higher performing gas turbine engines.

References

[1] Matsunuma, T., Abe, H., Tsutsui, Y., and Murata, K., 1998, "Characteristics of an Annular Turbine Cascade at Low Reynolds Numbers.", presented at IGTI 1998 in Stockholm, Sweden, June 1998, paper #98-GT-518.

[2] Sharma, O., 1998, "Impact of Reynolds Number on LP Turbine Performance," *Proc. Of 1997 Minnowbrook II Workshop on Boundary Layer Transition in Turbomachines*, NASA/CP-1998-206958.

[3] Zhang, X., and Hodson, H., "The Combined Effects of Surface Trips and Unsteady Wakes on the Boundary Layer Development of an Ultra-High-Lift LP Turbine Blade," *ASME Turbo Expo 2004: Power for Land, Sea, and Air,* GT2004-53081.

[4] Zhang, X., and Hodson, H., "Separation and Transition Control on an Aft-loaded Ultra-High-Lift LP Turbine Blade at Low Reynolds Numbers: Low-Speed Investigation," *ASME Turbo Expo 2005: Power for Land, Sea, and Air,* GT2005-68892.

[5] Rivir, R.B., Sondergaard, R., Bons, J.P., and Lake, J.P., 2000, "Passive and Active Control of Separation in Gas Turbines", presented at AIAA Fluids 2000 in Denver CO, 19-22 June, 2000, AIAA paper #2000-2235.

[6] Bons, J. P., Sondergaard, R., and Rivir, R. B., "The Fluid Dynamics of LPT Blade Separation Control Using Pulsed Jets," *ASME Journal of Turbomachinery*, Vol. 124, Jan. 2002, pp. 77-85.

[7] Volino, R. J., "Separation Control on Low-Pressure Turbine Airfoils Using Synthetic Vortex Generator Jets," *Proceedings of ASME Turbo Expo 2003: Power for Land, Sea, and Air*, GT2003-38729.

[8] Eldredge, R. G., and Bons, J. P., 2004, "Active Control of a Separating Boundary Layer with Steady Vortex Generating Jets—Detailed Flow Measurements," presented at the AIAA Aerospace Sciences Meeting, Reno, Nevada, Jan. 5-8, 2004.

[9] Hansen, L. C. and Bons, J. P., 2004, "Time-Resolved Flow Measurements of Pulsed Vortex-Generator Jets in a Separating Boundary Layer," *AIAA J. Propulsion and Power,* Vol. 22, No 3, May-June 2006, pp. 558-566.

[10] Postl, D., Gross, A., and Fasel, H. F., 2003, "Numerical Investigation of Low-Pressure Turbine Blade Separation Control," AIAA 2003-0614.

[11] Postl, D, Gross, A., and Fasel, H. F., 2004, "Numerical Investigation of Active Flow Control for Low-Pressure Turbine Blade Separation," AIAA 2004-0750.

[12] Ozturk, B., Schobeiri, M. T., "Effect of Turbulence Intensity and Periodic Unsteady Wake Flow Condition on Boundary Layer Development, Separation, and Re-attachment over the Separation Bubble along the Suction Surface of a Low Pressure Turbine Blade," *ASME Turbo Expo 2006: Power for Land, Sea and Air,* GT2006-91293.

[13] Stieger, R., Hollis, D., Hodson, H., "Unsteady Surface Pressures Due to Wake Induced Transition in a Laminar Separation Bubble on a LP Turbine Cascade," *Proceedings of ASME Turbo Expo 2003: Power for Land, Sea, and Air,* GT2003-38303.

[14] Gostelow, J.P. and Thomas, R.L., 2003, "Response of a Laminar Separation Bubble to an Impinging Wake," *Proceedings of ASME Turbo Expo 2003: Power for Land, Sea, and Air,* GT2003-38972.

[15] Thomas, R. L., Gostelow, J. P., "The Pervasive Effect of the Calmed Region," *Proceedings of ASME Turbo Expo 2005: Power for Land, Sea and Air,* GT2005-69125.

[16] Funazaki, K., Wakita, Y., and Otsuki, T., "Studies on Bypass Transition of a Boundary Layer Subjected to Localized Periodic External Disturbances," *Proceedings of ASME Turbo Expo 2004: Power for Land, Sea, and Air,* GT2004-53305.

[17] Funazaki, K., Koyabu, E., "Studies on Wake-Induced Bypass Transition of Flate-Plate Boundary Layers under Pressure Gradients and Free-Stream Turbulence," *Proceedings of ASME Turbo Expo 2006: Power for Land, Sea and Air,* GT2006-91103.

[18] Cattanei, A., Zunino, P., Schroder, T., Stoffel, B., and Matyschok, B., "Detailed Analysis of Experimental Investigations on Boundary Layer Transition in Wake Disturbed Flow," *Proceedings of ASME Turbo Expo 2006: Power for Land, Sea and Air,* GT2006-90128.

[19] Mayle, R. A., "The Role of Laminar-Turbulent Transition in Gas Turbine Engines," *ASME Journal of Turbomachinery,* Vol. 113, Oct. 1991, pp. 509-537.

[20] Volino, R.J., Schultz, M.P., and Pratt, C.M., 2003, "Conditional Sampling in a Transitional Boundary Layer Under High Freestream Turbulence Conditions," ASME Journal of Turbomachinery, Vol. 125, pp. 28-36.

[21] Clark, J. P., 2004, "An Integrated Design, Analysis, and Optimization System for Turbine Airfoils," AFRL Internal Report.

[22] Rao, K.V., Delaney, R.A., and Topp, D.A., “Turbine Vane-Blade Interaction: Vol. 1,2-D Euler/Navier-Stokes Aerodynamic and Grid Generation Developments,” U.S. Air Force Research Lab., Rept. WL-TR-94-2073, Wright-Patterson AFB, OH, Jan. 1994.

[23] Bons, J. P., Hansen, L. C., Clark, J.P., Koch, P.J., and Sondergaard, R., 2005, “Designing Low-Pressure Turbine Blades with Integrated Flow Control,”*Proceedings of ASME Turbo Expo 2005: Power for Land, Sea, and Air*, GT2005-68962.

[24] Townsend, A.A., 1948, “Local Isotropy in the Turbulent Wake of a Cylinder,” Australian Journal of Scientific Research, Vol. 1, pp. 161-174.

[25] Praisner, T. J. and Clark, J. P., 2004, "Predicting Transition in Turbomachinery, Part 1- A Review and New Model Development," ASME Paper No. GT-2004-54108.

[26] Sondergaard, R., Bons, J. P., and Rivir, R. B., 2002, “Control of Low-Pressure Turbine Separation Using Vortex Generator Jets,” *AIAA J. Propulsion and Power*, Vol. 18, No. 4, Jul/Aug 2002. pp. 889-895.

[27] Stieger, R.D., and Hodson, H.P., 2003, “The Transition Mechanism of Highly-Loaded LP Turbine Blades,” *Proceedings of ASME Turbo Expo 2003: Power for Land, Sea, and Air*, GT2003-38304.

[28] Bloxham, M. Reimann, D., and Bons, J.P., 2006, “The Effect of VGJ Pulsing Frequency on Separation Bubble Dynamics,” presented at the AIAA 44th Aerospace Sciences Meeting and Exhibit in Reno, NV, 9-12 Jan 2006 (paper #AIAA 2006-0876).

Appendix A. LabView Intermittency Program

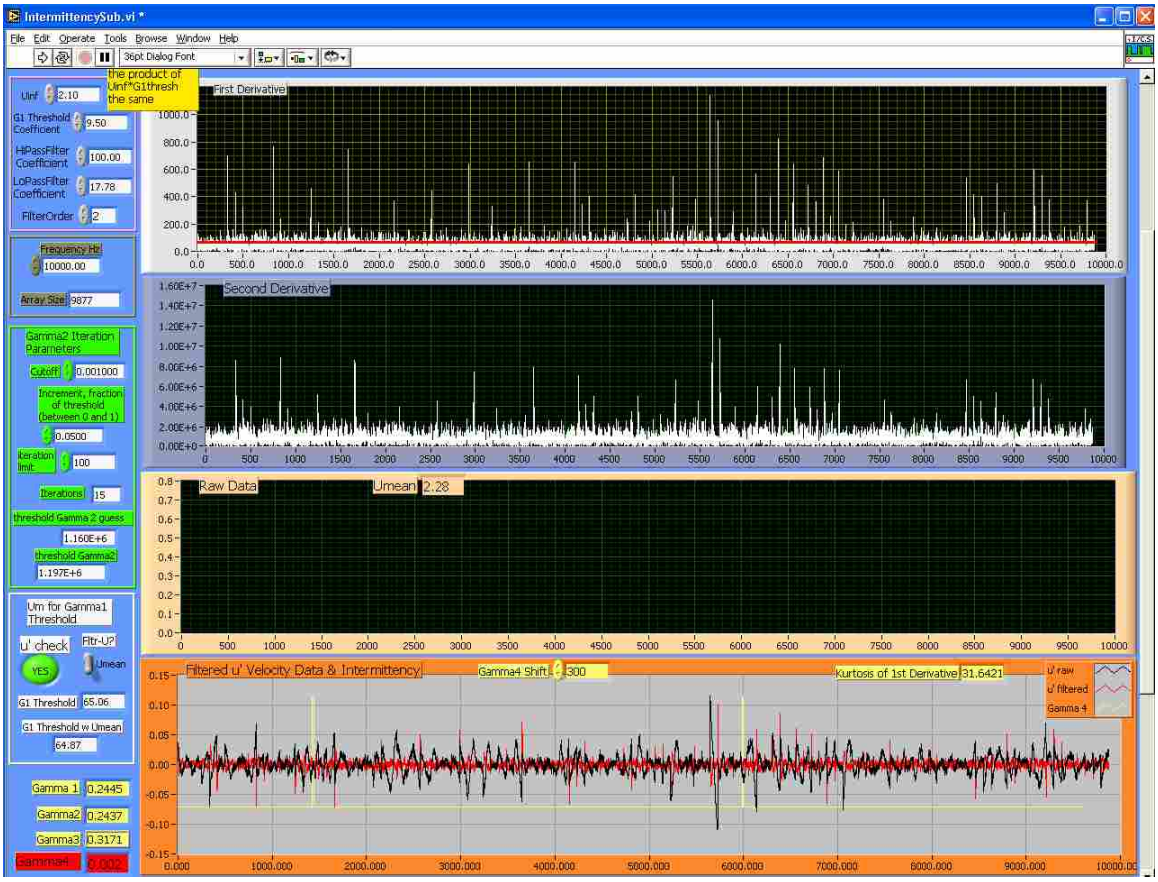

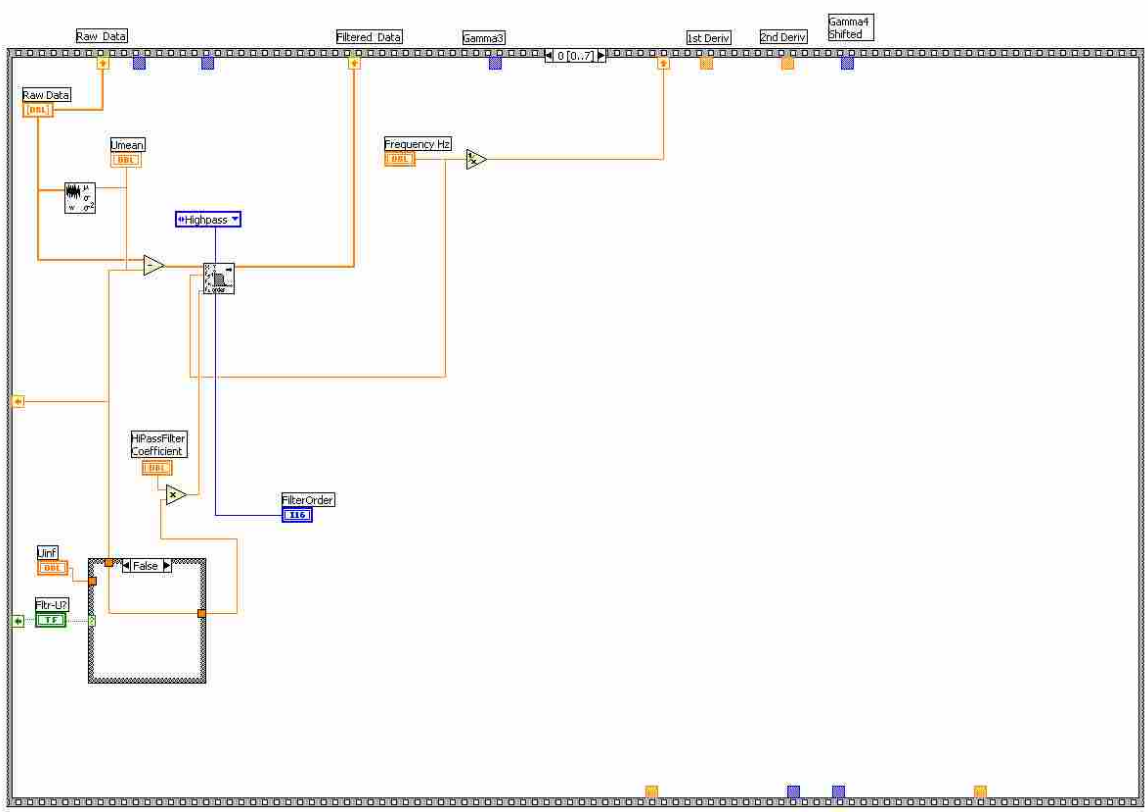
Raw Data
Filtered Data
Gamma3
0 [0..7]
1st Deriv
2nd Deriv
Gamma4 Shifted
Raw Data
Umean
Frequency Hz
Highpass
HiPassFilter Coefficient
FilterOrder
Uinf
False
Fltr-U?

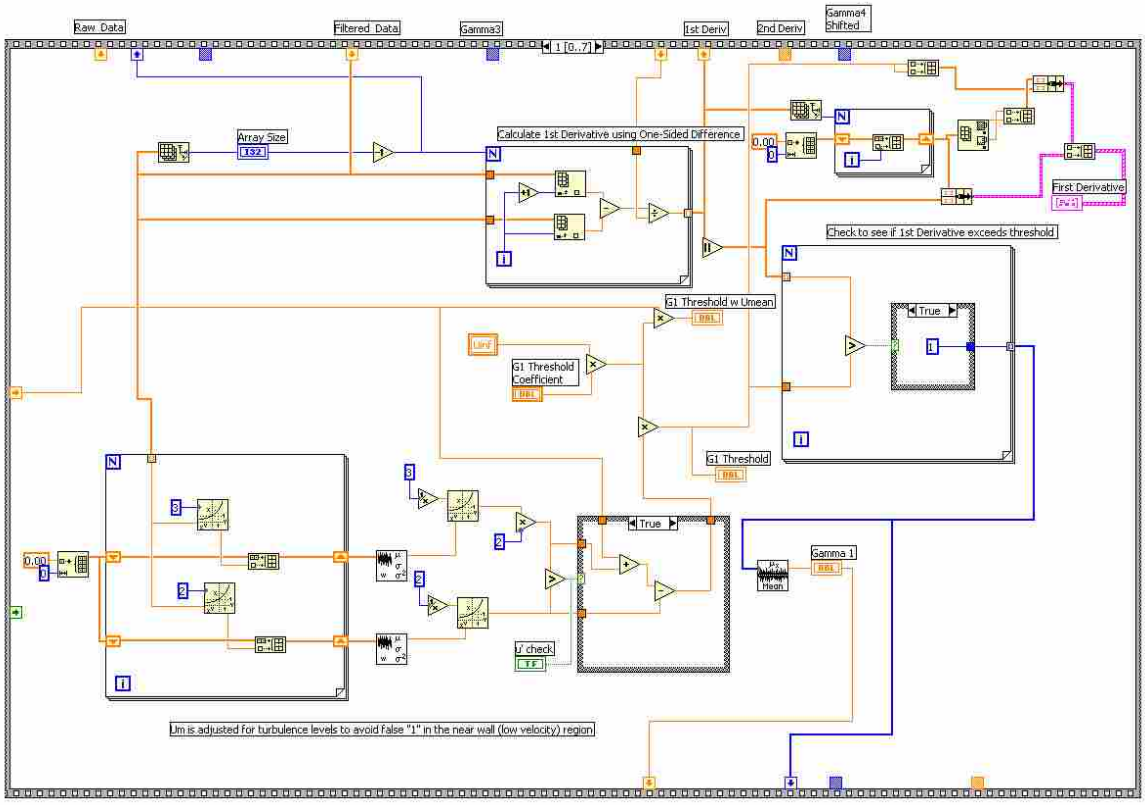
Raw Data
Filtered Data
Gamma3
1 [0..7]
1st Deriv
2nd Deriv
Gamma4 Shifted
Array Size
Calculate 1st Derivative using One-Sided Difference
First Derivative
Check to see if 1st Derivative exceeds threshold
G1 Threshold w Umean
G1 Threshold Coefficient
G1 Threshold
True
Gamma 1
U check
Um is adjusted for turbulence levels to avoid false "1" in the near wall (low velocity) region

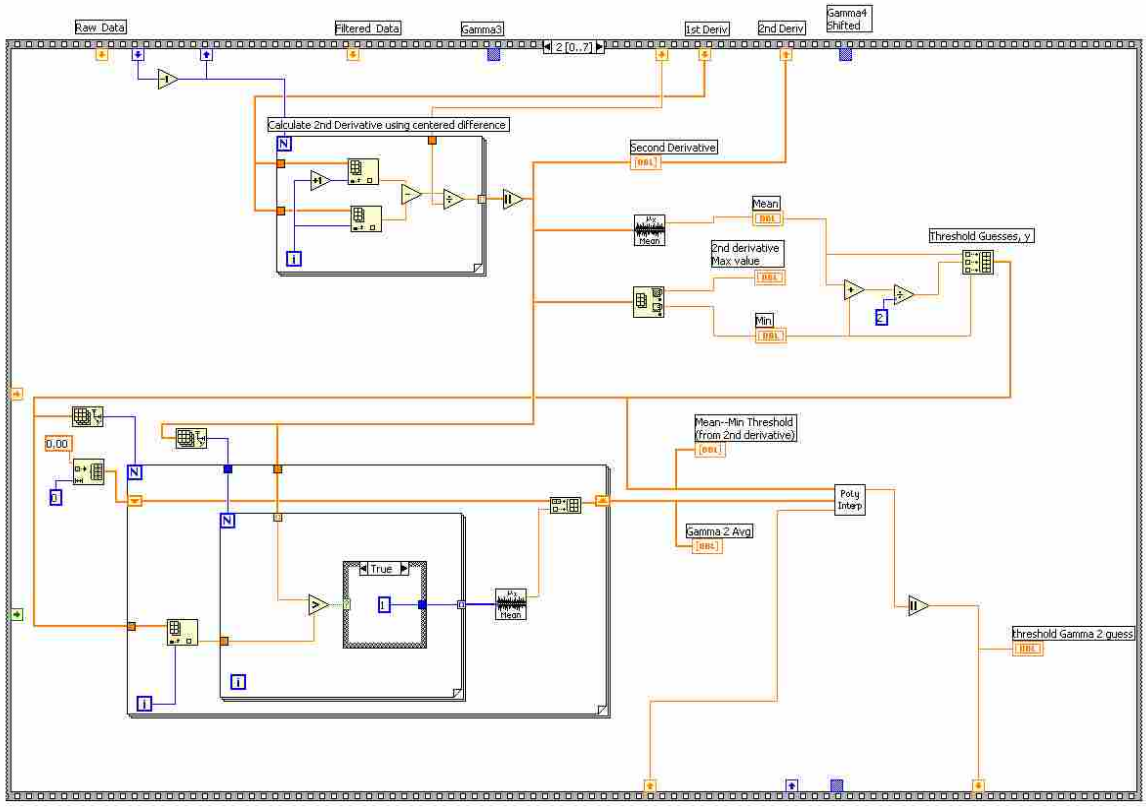
Raw Data
Filtered Data
Gamma3
2 [0..7]
1st Deriv
2nd Deriv
Gamma4 Shifted
Calculate 2nd Derivative using centered difference
Second Derivative
Mean
2nd derivative Max value
Min
Threshold Guesses, y
0.00
Mean--Min Threshold (from 2nd derivative)
Poly Interp
Gamma 2 Avg
True
Threshold Gamma 2 guess

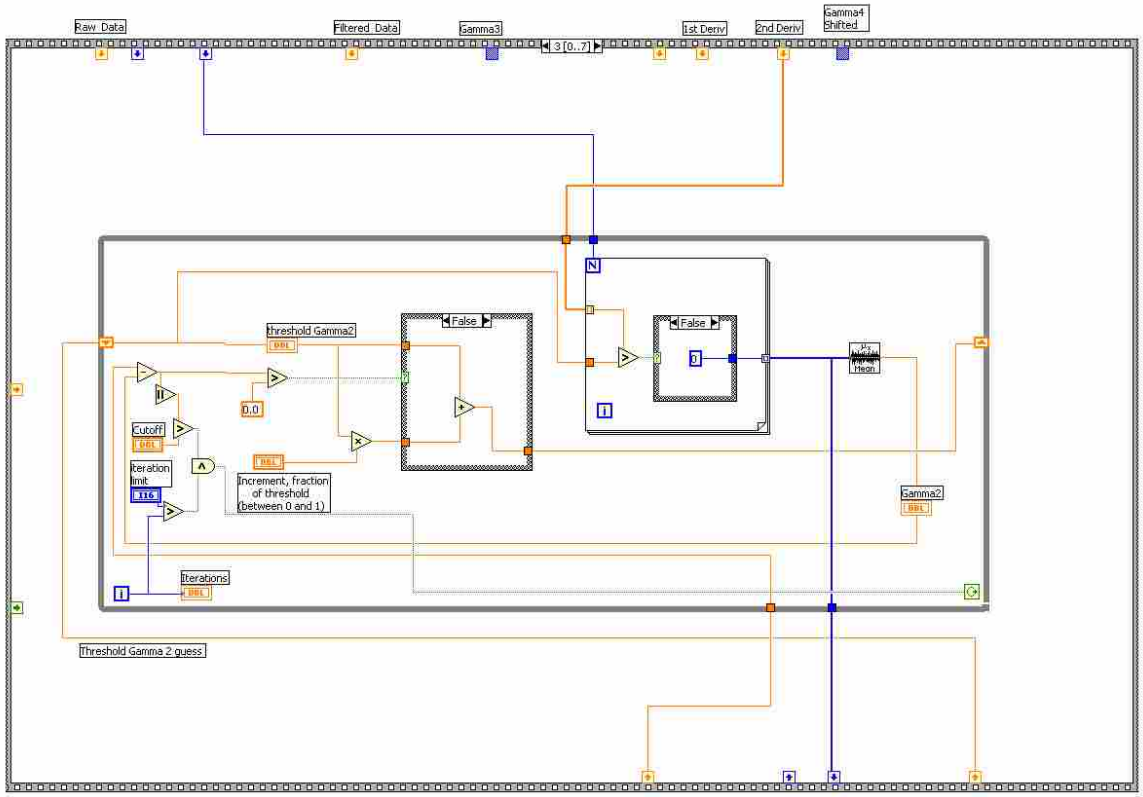
Raw Data
Filtered Data
Gamma3
3 [0..7]
1st Deriv
2nd Deriv
Gamma4 Shifted
Threshold Gamma2
False
False
0.0
Cutoff
Iteration limit
Increment, fraction of threshold (between 0 and 1)
Gamma2
Iterations
Threshold Gamma 2 guess

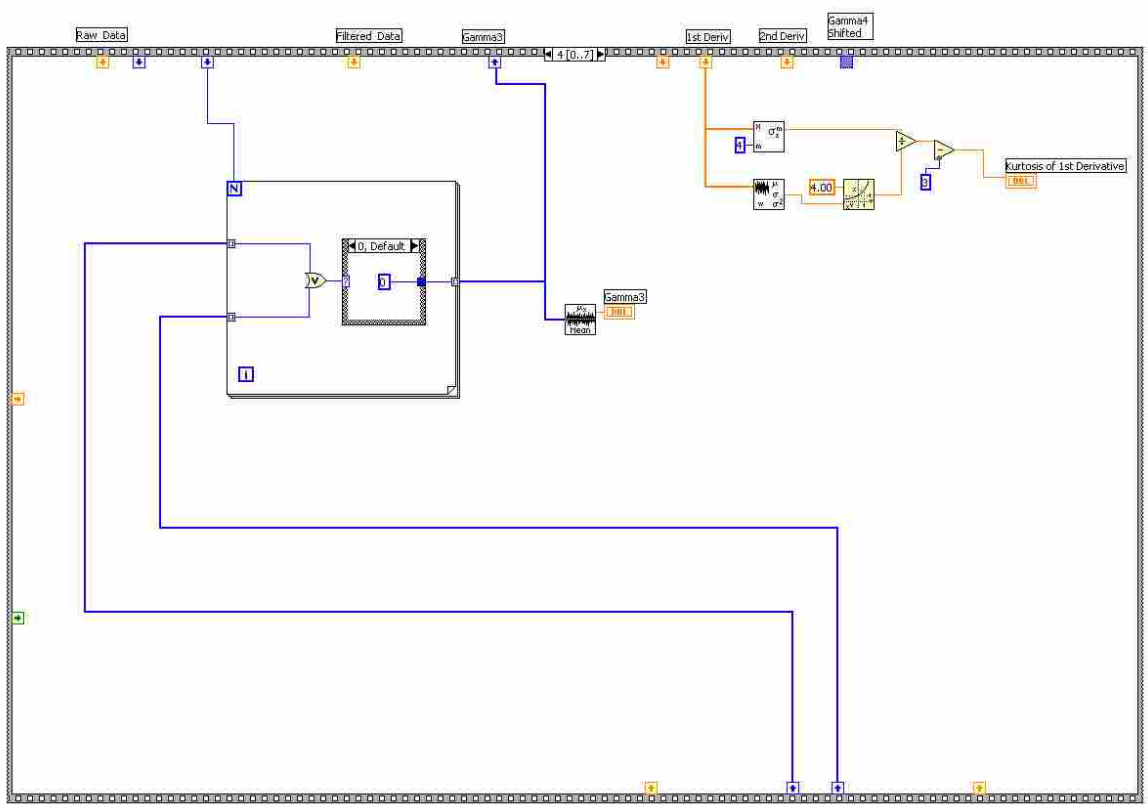
Raw Data
Filtered Data
Gamma3
4 [0..7]
1st Deriv
2nd Deriv
Gamma4 Shifted
Kurtosis of 1st Derivative
0, Default
Gamma3
Mean
4.00

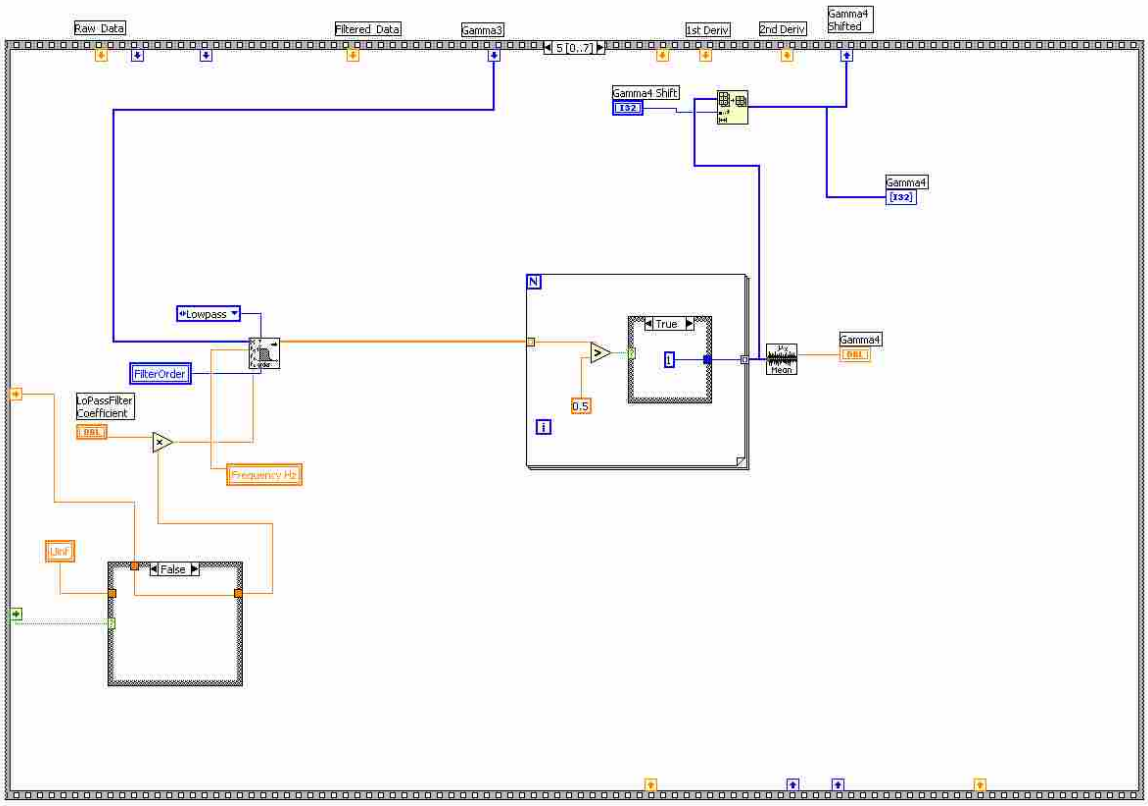
Raw Data
Filtered Data
Gamma3
5 [0..7]
1st Deriv
2nd Deriv
Gamma4 Shifted
Gamma4 Shift
I32
Gamma4
[I32]
"Lowpass
FilterOrder
LoPassFilter Coefficient
DBL
Frequency Hz
True
0.5
Mean
Gamma4
DBL
Unif
False

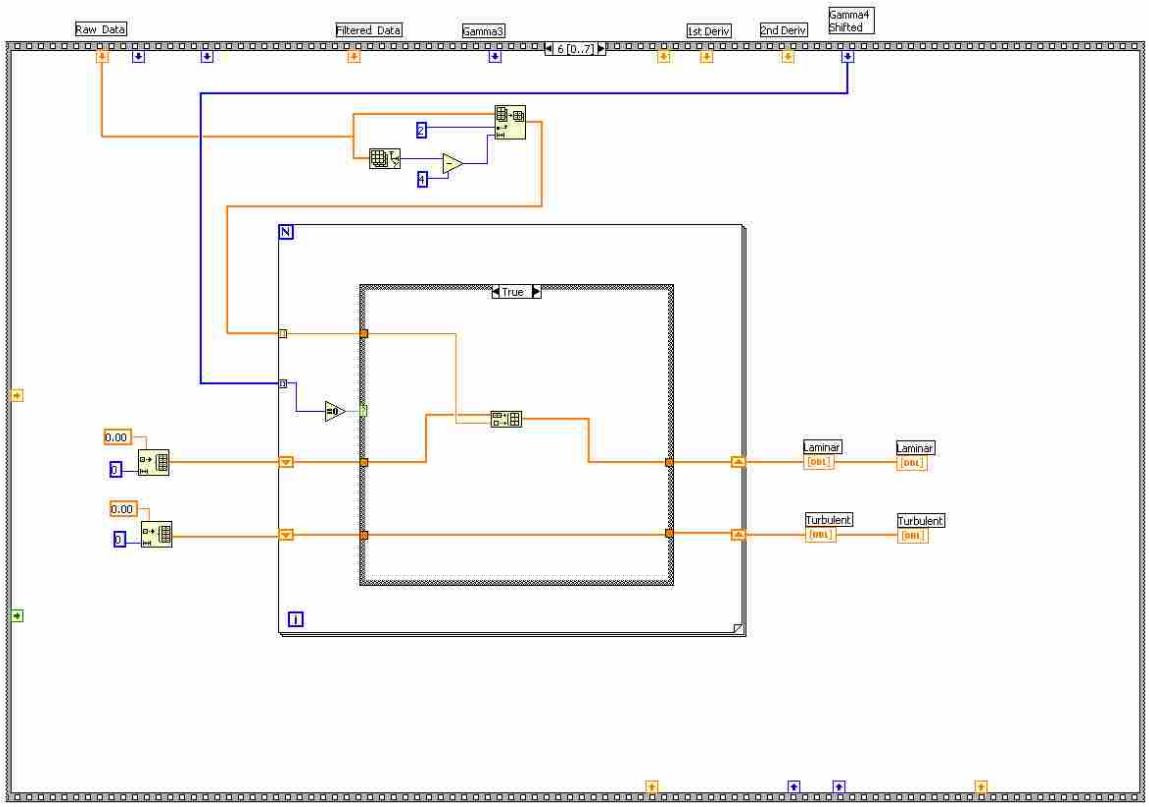
Raw Data
Filtered Data
Gamma3
6 [0..7]
1st Deriv
2nd Deriv
Gamma4 Shifted
2
4
N
True
0.00
0
Laminar
Laminar
Turbulent
Turbulent
i

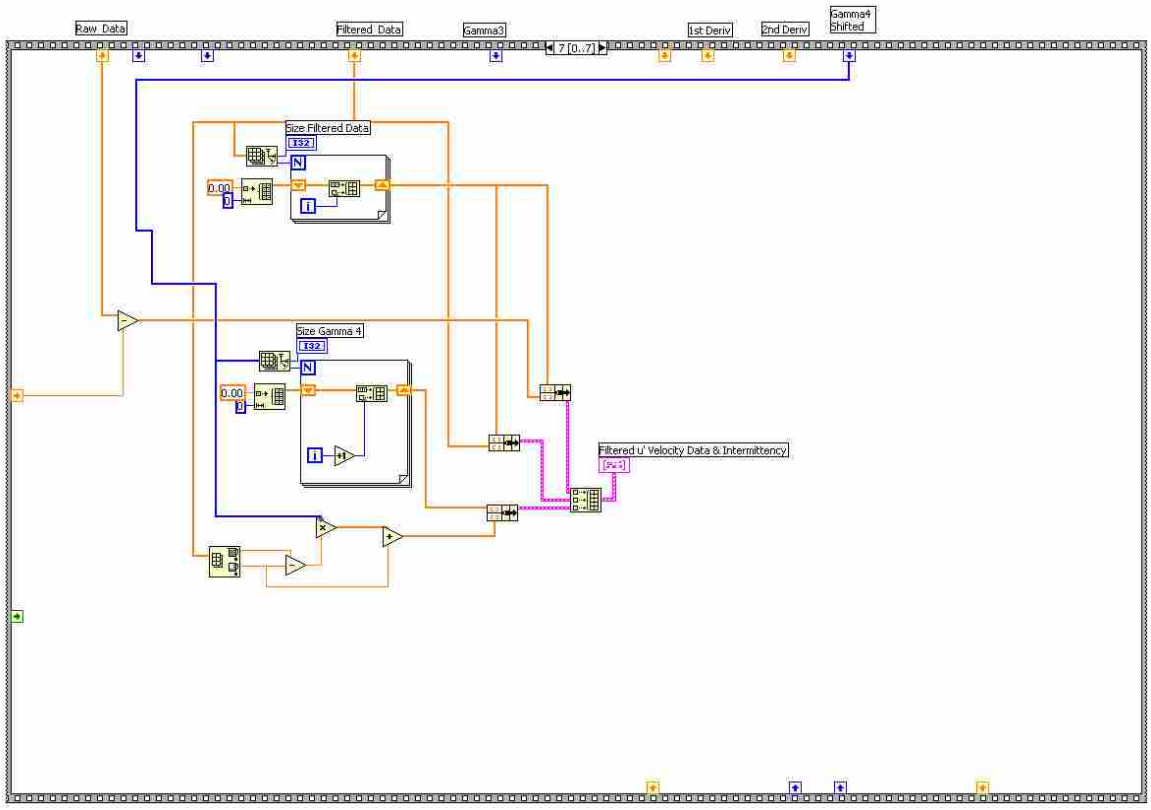
Raw Data
Filtered Data
Gamma3
7 [0..7]
1st Deriv
2nd Deriv
Gamma4 Shifted
Size Filtered Data
I32
N
0.00
0
i
Size Gamma 4
I32
N
0.00
0
i
Filtered u' Velocity Data & Intermittency
[P×1]